Master's thesis

NTNU
Norwegian University of Science and Technology
Faculty of Information Technology and Electrical Engineering
Department of Engineering Cybernetics

Håkon Syverud Fadum

The Generalized Super-Twisting Algorithm Used for Robust Control of Unmanned Subsea Vehicles Operating at Exposed Aquaculture Sites

Master's thesis in Industrial Cybernetics
Supervisor: Jan Tommy Gravdahl
Co-supervisor: Sveinung Johan Ohrem and Bent Oddvar Arnesen Haugaløkken
June 2022

NTNU
Kunnskap for en bedre verden

Håkon Syverud Fadum

The Generalized Super-Twisting Algorithm Used for Robust Control of Unmanned Subsea Vehicles Operating at Exposed Aquaculture Sites

Master's thesis in Industrial Cybernetics
Supervisor: Jan Tommy Gravdahl
Co-supervisor: Sveinung Johan Ohrem and Bent Oddvar Arnesen
Haugaløkken
June 2022

Norwegian University of Science and Technology
Faculty of Information Technology and Electrical Engineering
Department of Engineering Cybernetics

NTNU
Norwegian University of
Science and Technology

Abstract

Aquaculture fish farming is a rapidly growing industry both domestically and globally. In Norway, there exists an industry incentive to be able to use environmentally exposed coastal regions for aquaculture fish farms for environmental and spatial reasons. This creates a range of technical challenges for the industry, as the environmental disturbances and logistical challenges at exposed sites create a difficult farming environment compared to sheltered sites. Therefore, there exists a need to develop technology able to manage the challenges that the exposed sites present. One of these technologies is robust control systems for autonomous vehicles, able to withstand the time-varying environmental disturbances experienced at exposed sites. This thesis aims to improve the robustness of the control systems used in remotely operated vehicle (ROV) operations performed at exposed aquaculture fish farms, using higher-order sliding-mode (HOSM) techniques. Such robust systems make day-to-day ROV operations at exposed sites less dependent on calm environmental conditions and human intervention.

This thesis resulted in two controller types allowing for robust three-dimensional maneuvering of an ROV. The controllers are based on the generalized super-twisting algorithm (GSTA), which is a well-performing second-order HOSM technique. The first controller type uses fixed gains while the second tests an adaption law never before used for this use case. Both controllers have been verified through numerical simulations and evaluated using the ARGUS Mini ROV at the SINTEF ACE full-scale aquaculture laboratory. The simulations showed that the controllers were able to accurately traverse the net pen while exposed to wave and current loads similar to what can be seen at ACE. The field test verified these results and showed that the controllers were able to track a net pen accurately at a site with large disturbances. A comparison between both GSTA controller types and a PID controller was completed using the field test results, where both GSTA-based control methods outperformed conventional PID control for controllers in three out of four degrees of freedom (DOF).

Sammendrag

Fiskeoppdrett er en industri i stor vekst. Den norske fiskeoppdrettsindustrien ønsker å utnytte eksponerte havbrukslokasjoner for fiskeoppdrett. Dette er på grunn av forskjellige miljø og plassproblemer som industrien opplever ved de mindre miljøutsatte kystområdene. Eksponerte kystområder har logistiske og driftsmessige utfordringer som gjør det vanskelig å drive effektivt fiskeoppdrett. En av disse utfordringene er at fiskeoppdrettsanlegg i åpent hav er eksponert mot store bølger og havstrømmer. Dette gir store og uforutsigbare miljøpåvirkninger på fartøyene som brukes til inspeksjon av fiskemerdene. Formålet med denne oppgaven er å utvikle regulatorer basert på høyere-ordens sliding-mode (HOSM) teknikker for manøvrering av et ubemannet undervannsfartøy i tre dimensjoner. Disse regulatorene er robuste mot ikke-modellerte miljøpåvirkninger og modelleringsfeil. Dette tillater nøyaktig merdfølging med ubemannede farkoster, samt gjør det mulig å uføre daglige operasjoner ved oppdrettsanlegg under store miljøpåvirkninger.

Arbeidet utført under dette prosjektet førte til to forskjellige regulatorer basert på den generaliserte super-twisting algoritmen (GSTA). GSTA er en andre-ordens HOSM algoritme som generelt er god på å håndtere ikke-modellerte forstyrrelser og parametriske feil. Den første regulator-typen tar i bruk faste regulatorparametere, mens den andre typen bruker adaptive regulatorparametere. Den adaptive versjonen har aldri tidligere blitt brukt innen dette bruksområdet. Begge kontrollerne klarer å manøvrere et undervannsfartøy i tre dimensjoner under utfordrerne miljøforhold. Ytelsen til regulatorene ble først verifisert gjennom simulering. Deretter ble de testet ved SINTEF ACE fullskala havbrukslaboratorium, som består av fiskemerder i et åpent havområde utenfor Frøya. Simuleringene viste at begge regulatortypene håndterte normale værforhold ved ACE. Under den fysiske testen var miljøpåvirkningen i merden store, men de GSTA-baserte regulatorene klarte likevel å følge fiskemerden på ønsket avstand. Fysiske eksperimenter med PID-kontrollere ble også gjennomført. Begge GSTA-typene ga bedre resultater enn PID i tre av fire frihetsgrader.

Preface and Acknowledgements

This thesis is conducted as the final requirement for the 2-year MSc program Industrial Cybernetics at the Norwegian University of Science and Technology (NTNU). The project, spanning from January to June 2022, has been supervised by Professor Jan Tommy Gravdahl and co-supervised by Dr. Sveinung Johan Ohrem and Dr. Bent Oddvar Arnesen Haugaløkken. The thesis is a collaboration with SINTEF Ocean, where SINTEF Ocean has provided access to relevant simulation objects, access their simulation software FhSim, as well as the equipment and funding necessary to perform field validation of the project results. A scientific paper will be written in collaboration with Professor Gravdahl, Dr. Ohrem, and Dr. Haugaløkken based on the results of this thesis.

The project ended in a field test at the SINTEF ACE full-scale marine laboratory. I would like to thank Ph.D. student Herman Bjørn Amundsen for helping me update the software to be compatible with the interface and hardware used during the field test. Due to a slim weather window, I was unfortunately not able to join the tests myself. I would therefore like to thank Amundsen, Ohrem, and Haugaløkken for performing the field tests on my behalf. They took time out of their own experiments and provided valuable result data to the project. I would also like to thank SINTEF for giving this project the resources required to perform the field tests.

This project has been both exciting and educational. I am grateful for the opportunity to contribute to this exciting thesis and would therefore like to thank Dr. Walter Caharija and Professor Gravdahl for entrusting me with it. I would also like to thank Professor Gravdahl, Ohrem, Haugaløkken, and Amundsen for their discussions and counseling, helping me steer the project in an exciting direction. Finally, I would like to thank my family for their unconditional support throughout my entire education, and my friends for making the last few years memorable.

June 2022. Trondheim, Norway

Håkon Syverud Fadum

Contents

List of Tables

List of Figures

List of Abbreviations

ROV	Remotely Operated Vehicle
DOF	Degrees of Freedom
NED	North-East-Down
CO	Coordinate Origin
CG	Center of Gravity
CB	Center of Buoyancy
GAS	Globally Asymptotically Stable
RMSE	Root-mean-square Error
PID	Propotional-integral-derivative
SMC	Sliding Mode Control
HOSM	Higher Order Sliding Mode
STA	Super-Twisting Algorithm
GSTA	Generalized Super-Twisting Algorithm
DVL	Doppler Velocity Log
RAO	Response Amplitude Operators
LOS	Line-of-sight
ILOS	Integral Line-of-sight

Part I

Introduction

Chapter 1

Introduction

1.1 Motivation

Aquaculture fish farming is a rapidly growing industry. In 2021 the Norwegian aquaculture industry sold 1.64 million metric tons of marketable fish meat valued at 80.5 billion NOK [1]. This is a new record breaking year for the industry, following a rising trend in production and sales. The aquaculture industry in Norway has grown to be a major employer in regional areas of the country, supporting the population in fjords and coastal areas [2]. In addition to the monetary aspects, aquaculture fish farming plays an important role in fulfilling an increasing global demand for food [3]. According to the world bank 62% of the seafood consumed globally will be farm raised by 2030 [2]. Further development of the Norwegian aquaculture industry could provide a valuable addition to the Norwegian economy while at the same time help sustain a growing global population.

A major interest within the Norwegian aquaculture industry is utilizing coastal locations exposed the the open sea for fish farming. One of the reasons for this desire is that the sheltered coastal regions used in aquaculture fish farming, e.g. fjords, are of limited number, therefore limiting production [2, 3]. This makes the ability to use exposed locations advantageous to the industry growth. Another benefit of using exposed locations is the higher exchange of water in exposed locations. This helps dilute waste produced by the farm and helps prevent rapid spread of diseases, ultimately increasing fish welfare and decreasing environmental impact [3]. Additionally, using locations further away from the wild fish population would also help prevent ecological issues created by sea lice and escaped farm fish [2]. However, moving the farms creates new challenges for the industry. One of these challenges is the increased exposure to wind-, wave-, and current loads. These environmental conditions can cause issues with the monitoring and daily routine operations done at fish farms. An improvement needed to effectively make use of exposed fish farms are autonomous systems able to perform operations under such conditions [2]. Therefore, a necessary technological development are robust systems able to handle the time-varying disturbances experienced at exposed coastal locations.

This thesis aims to improve the robustness of the control systems used in remotely operated vehicle (ROV) operations performed at exposed aquaculture fish farms, with

respect to time-varying disturbances. The project is a collaboration between NTNU and SINTEF Ocean. It builds on parts of the research done during SINTEF's Artifex project which was a project exploring new ways of conducting operations at aquaculture fisheries [4]. This thesis aims to create controllers allowing for robust three-dimensional maneuvering of an ROV. This is done using a higher order sliding mode (HOSM) based control system, specifically the generalized super-twisting algorithm (GSTA). This controller type, and sliding mode control (SMC) in general, is known for its robustness to unmodeled dynamics and disturbances. The proposed controllers are validated through simulation before proceeding to a field test. The field test results are then compared to another conventional control method, giving insight into the proposed controller performance relative to another control system. An improvement in controller robustness could help improve operations at exposed aquaculture sites and may lead to an expanded weather window in which operations can be done.

1.2 Problem Description

The purpose of this thesis is to create a control system based on HOSM theory allowing for robust control of an ROV. The controller design should test some new variation of an HOSM technique which has not previously been tested for this use case. The controllers should be able to track an aquaculture net pen while affected by time-varying environmental disturbances. These controllers should be proven stable analytically, through simulation, and through a field test at the SINTEF ACE full-scale aquaculture laboratory. The goals can be summarized as the following:

- Develop HOSM controllers for four degrees of freedom (DOF) allowing for robust three-dimensional maneuvering of an ROV.
- Implement the derived controllers into MATLAB and/or FhSim and create a simulation environment able to simulate operations at an aquaculture fish farm.
- Validate the developed controllers' stability theoretically.
- Validate the developed controllers' stability and performance through simulation.
- Perform a field validation of the controllers at the SINTEF ACE full-scale marine laboratory using the Argus MINI ROV to test the controllers' performances, in collaboration with SINTEF OCEAN.

1.3 Contributions

This thesis presents both fixed gain and adaptive gain variations of surge, sway, heave, and yaw controllers based on the generalized super-twisting algorithm (GSTA). The adaptive gain variation is based on an adaption law, developed in [5], which has never previously been used for control design on an ROV. These controllers are validated theoretically, thorough simulations, and through a field test. Their performances are compared to each other and a PID controller. The contributions can be summarized as the following:

1. Fixed- and adaptive gain GSTA controllers for three dimensional maneuvering of an ROV.
2. Theoretical stability validation of the controllers based on general GSTA stability theorems.
3. Simulation performance validation of both developed controllers controllers.
4. Field test performance validation of the controllers, including a performance comparison to a PID controller.

1.4 Project Outline

The project is made up of the following parts and chapters:

- Part II presents background theory relevant to this thesis:
  - Chapter 2 presents basic marine craft theory describing mainly notation, underwater vehicle models, actuation, and environmental effects.
  - Chapter 3 presents a general theory on guidance systems, reference generation, and signal estimation.
  - Chapter 4 presents control system theory for controllers relevant to this thesis.
  - Chapter 5 presents the most relevant previous work completed, which this thesis will build upon.
- Part III presents this thesis' method:
  - Chapter 6 describes the dynamical models used in the thesis.
  - Chapter 7 derives the controllers designed in this thesis and shows their respective stability proofs.
- Part IV presents and discusses the results of the thesis:
  - Chapter 8 presents the simulation test setup used and the simulation results.
  - Chapter 9 presents the field test setup used and the results of the field test.
  - Chapter 10 discusses the results found in Chapter 8 and Chapter 9, alongside a few other notable results from the thesis.
- Part V is the thesis conclusion:
  - Chapter 11 concludes the work done in this thesis and suggests what further work can be done to build upon it.
- The appendices present relevant attachments referenced at some point in the thesis.

Part II

Theory

Chapter 2

Marine Craft Theory

This chapter presents the fundamental theory used in mathematical modeling of marine crafts. The models are used to perform simulations, and to develop control algorithms. In particular, theory regarding remotely operated vehicles (ROVs) is introduced. The dynamic equations that describe the marine systems are important as they bring about awareness of how such systems function, as well as provide the basis for simulation and control design [6, Chapter 1.1]. Dynamical models of physical systems can vary depending on the model development process and the model's intended purpose. For instance, a high-fidelity simulation model will vary from a control design model and an estimator model as each model has different requirements for the number of states, model accuracy, simplicity, and other influencing parameters [6, Chapter 1.1]. For further reading on the modeling of marine vehicles, the reader is referred to [6, 7].

2.1 Frames of Reference

Note: This section (2.1) is taken directly from the project report [8, Chapter 4.1]. It is included in this thesis as it is relevant and the thesis directly builds on that previous work.

It is convenient to have several reference frames when describing the motion of a marine craft. These frames are used to express the varying movements, forces, and positions of the system and are essential when trying to understand the dynamics of marine vehicles. Two frames stand out as important when analyzing the local dynamics of a marine craft. [6]

North-East-Down (NED): NED is a reference frame denoted by $\{n\} = (x_n, y_n, z_n)$ where the x-axis points to the true north, the y-axis points towards the east and the z-axis points downwards normal to the Earth's surface [6]. This plane can be visualized as a tangent plane at any given point on Earth's surface. It is a flat-earth model and is therefore only accurate within approximately 10×10 km of the reference frame origin (o_n). A common simplification, which is done in this thesis, is to consider NED an inertial frame. [6]

BODY: BODY is a reference frame denoted by $\{b\} = (x_b, y_b, z_b)$ with the coordinate origin o_b fixed to a vehicle. This reference frame is moving with the vehicle it is attached to. In this reference frame, the x-axis is the vehicle's longitudinal axis, the y-axis is the vehicle's transversal axis, and the z-axis is the vehicle's normal axis (from top to bottom). [6]
[8, Chapter 4.1]

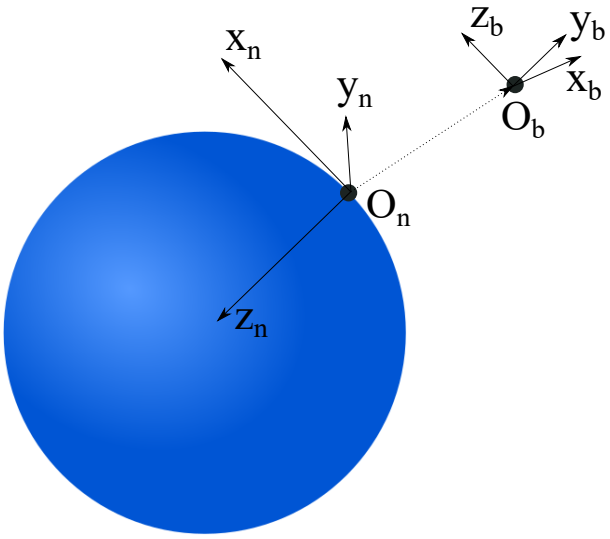

Figure 2.1: Visualization of Reference Frames, Inspired by [6, Figure 2.2] & [9, Figure 2.1]

2.2 SNAME Naming Convention

Note: This section (2.2) is taken directly from the project report [8, Chapter 4.2]. It is included in this thesis as it is relevant and the thesis directly builds on that previous work.

This report makes use of the naming convention used by The Society of Naval Architects and Marine Engineers as they are presented in [6]. Table 2.1 presents the naming convention for a marine craft moving in 6 degrees of freedom (DOF). [8, Chapter 4.2]

	BODY			**NED**
DOF		Forces and moments	Linear and angular velocities	Positions and Euler angles
1	Motion in the x_b direction (surge)	X	u	x^n
2	Motion in the y_b direction (sway)	Y	v	y^n
3	Motion in the z_b direction (heave)	Z	w	z^n
4	Rotation about the x_b axis (roll)	K	p	ϕ
5	Rotation about the y_b axis (pitch)	M	q	θ
6	Rotation about the z_b axis (yaw)	N	r	ψ

Table 2.1: SNAME Naming Convention [6, Table 2.1]

2.3 Important Definitions

A few definitions are important when describing marine crafts. The most relevant ones for this project are shown in this chapter. These definitions are sourced from [6] and are included to help the reader understand the terms and notation used in the thesis.

Definition 2.1 (**Yaw or Heading Angle**). *"The angle ψ from the x_n axis (true North) to the x_b axis of the craft, positive around the z_n axis by the right-hand screw convention."* - [6, Definition 2.4]

Definition 2.2 (**Course Angle**). *"The angle χ from the x_n (true North) to the velocity vector of the craft, positive around the z_n axis by the right hand screw convention."* - [6, Definition 2.5]

Definition 2.3 (**CG relative CO**). *The position of the center of gravity (CG) is defined as $\boldsymbol{r_{bg}^b} \coloneqq [x_g, y_g, z_g]^T$ relative to the coordinate origin (CO).* [6, p. 21]

Definition 2.4 (**CB relative CO**). *The position of the center of buoyancy (CB) is defined as $\boldsymbol{r_{bb}^b} \coloneqq [x_b, y_b, z_b]^T$ relative to the CO.* [6, p. 21]

2.4 Kinematics

The 6-DOF kinematic equations for a marine craft can be expressed as:

$$\begin{gathered} \dot{\boldsymbol{\eta}} = \boldsymbol{J_\Theta}(\boldsymbol{\eta})\boldsymbol{\nu} \\ \Updownarrow \\ \begin{bmatrix} \dot{\boldsymbol{P}}_{\boldsymbol{nb}}^{\boldsymbol{n}} \\ \dot{\boldsymbol{\Theta}}_{\boldsymbol{nb}} \end{bmatrix} = \begin{bmatrix} \boldsymbol{R}(\boldsymbol{\Theta}_{\boldsymbol{nb}}) & \boldsymbol{0_{3\times 3}} \\ \boldsymbol{0_{3\times 3}} & \boldsymbol{T}(\boldsymbol{\Theta}_{\boldsymbol{nb}}) \end{bmatrix} \begin{bmatrix} \boldsymbol{v}_{\boldsymbol{nb}}^{\boldsymbol{b}} \\ \boldsymbol{\omega}_{\boldsymbol{nb}}^{\boldsymbol{b}} \end{bmatrix} \end{gathered} \tag{2.1}$$

where $\boldsymbol{\eta} \in \mathbb{R}^6$ and $\boldsymbol{\nu} \in \mathbb{R}^6$ [6, eq. (2.53)]. A common simplification of Equation (2.1) is to assume small roll and pitch angles, i.e., $\phi = \theta \approx 0$. This reduces the number of DOF to 4, meaning $\boldsymbol{\eta} = [x, y, z, \psi]^T$. The 4-DOF kinematics can be expressed as:

$$\dot{\boldsymbol{\eta}} = \boldsymbol{J}(\boldsymbol{\psi})\boldsymbol{\nu} \tag{2.2}$$

where

$$\boldsymbol{J}(\boldsymbol{\psi}) \coloneqq \begin{bmatrix} \boldsymbol{R}_{\boldsymbol{z},\boldsymbol{\psi}} & 0 \\ 0 & 1 \end{bmatrix}$$

with $\boldsymbol{\eta} = [x^n, y^n, z^n, \psi]^T$ and $\boldsymbol{\nu} = [u, v, w, r]^T$ [6, p. 32]. Furthermore, for underwater vehicles neutral buoyancy can be assumed reducing the model to 3-DOF, meaning $\boldsymbol{\eta} = [x^n, y^n, \psi]^T$. [10] [6]

2.5 Kinetics

There are two main theories for studying the dynamics of marine vehicles. One way is through seakeeping models which study the motion of a marine vehicle at constant speed in the presence of waves. The other method is through maneuvering models which assume frequency-independent hydrodynamic coefficients and radiation-induced forces. This assumption in maneuvering theory allows for constant approximations of the added mass and potential damping which makes it unnecessary to calculate the fluid memory effects. This section presents a marine vehicle model based on maneuvering theory, where the hydrodynamic coefficients are approximated at one oscillation frequency. [6, p. 105, p. 135]

The 6-DOF kinetic equations for a marine vehicle can be expressed as:

$$\begin{aligned} \boldsymbol{M_{RB}}\dot{\boldsymbol{\nu}} + \boldsymbol{C_{RB}}(\boldsymbol{\nu})\boldsymbol{\nu} + \boldsymbol{M_A}\dot{\boldsymbol{\nu}}_{\boldsymbol{r}} + \boldsymbol{C_A}(\boldsymbol{\nu_r})\boldsymbol{\nu_r} + \boldsymbol{D}(\boldsymbol{\nu_r})\boldsymbol{\nu_r} + \boldsymbol{g}(\boldsymbol{\eta}) \\ = \boldsymbol{\tau} + \boldsymbol{\tau_{wind}} + \boldsymbol{\tau_{wave}} \end{aligned} \tag{2.3}$$

where $\boldsymbol{\nu_r}$ is the relative velocity vector, defined as $\boldsymbol{\nu_r} = \boldsymbol{\nu} - \boldsymbol{\nu_c}$, where $\boldsymbol{\nu_c} = [u_c, v_c, w_c, 0, 0, 0]^T$ and is irrotational [6, pp. 135-136]. The remaining parameter matrices, forces, and moments will be defined in the upcoming sections and are therefore not explained here.

2.5.1 Rigid Body Kinetics

The rigid-body system inertia matrix can be expressed on the form:

$$\boldsymbol{M_{RB}} = \begin{bmatrix} m\boldsymbol{I_3} & -m\boldsymbol{S}(\boldsymbol{r_{bg}^b}) \\ m\boldsymbol{S}(\boldsymbol{r_{bg}^b}) & \boldsymbol{I_b^b} \end{bmatrix} \tag{2.4}$$

where $\boldsymbol{M_{RB}}$ is a unique and satisfies:

$$\boldsymbol{M_{RB}} = \boldsymbol{M_{RB}^T} > 0, \qquad \dot{\boldsymbol{M}}_{\boldsymbol{RB}} = \boldsymbol{0_{6\times 6}}. \tag{2.5}$$

$\boldsymbol{I_b^b} = (\boldsymbol{I_b^b})^{\boldsymbol{T}} > 0$ is the vehicle inertia dyadic, $\boldsymbol{I_3} \in \mathrm{R}^{3\times 3}$ is the identity matrix, and $\boldsymbol{S}(\boldsymbol{r_{bg}^b})$ is a skew-symmetric matrix. [6, Property 3.1]

The Coriolis-centripetal terms are not unique and can have several representations. One of these representations is the Lagrangian parametrization. This representation uses $\boldsymbol{M_{RB}}$ to obtain:

$$\boldsymbol{C_{RB}}(\boldsymbol{\nu}) = \begin{bmatrix} \boldsymbol{0_{3\times 3}} & -m\boldsymbol{S}(\boldsymbol{\nu_1}) - m\boldsymbol{S}(\boldsymbol{S}(\boldsymbol{\nu_2})\boldsymbol{r_{bg}^b}) \\ -m\boldsymbol{S}(\boldsymbol{\nu_1}) - m\boldsymbol{S}(\boldsymbol{S}(\boldsymbol{\nu_2})\boldsymbol{r_{bg}^b}) & m\boldsymbol{S}(\boldsymbol{S}(\boldsymbol{\nu_1})\boldsymbol{r_{bg}^b}) - \boldsymbol{S}(\boldsymbol{I_b^b}\boldsymbol{\nu_2}) \end{bmatrix}. \tag{2.6}$$

where $\boldsymbol{\nu_1} = [u, v, w]^T$ and $\boldsymbol{\nu_2} = [p, q, r]^T$. Note that the representation of $\boldsymbol{C_{RB}}$ can always be made skew-symmetric [6, Property 3.2]. This is a useful property that can be used when designing nonlinear control systems. [6, pp. 65-67]

2.5.2 Hydrostatics

The hydrostatics, i.e., the restoring forces affecting an underwater vehicle can be expressed as:

$$W = mg, \qquad B = \rho g \nabla \tag{2.7}$$

where m is the vehicle mass including water, ∇ is the fluid volume the vehicle displaces, g is gravity, and ρ is the water density. [6, Chapter 4.1.1]

When designing underwater vehicles, it is common to give the vehicle a slight positive buoyancy ($B > W$). This makes the vehicle rise to the surface in case of a total system shutdown [6, p. 73]. The total hydrostatic forces acting on the vehicle can then be expressed as

$$\boldsymbol{g(\eta)} = \begin{bmatrix} (W-B)\sin(\theta) \\ -(W-B)\cos(\theta)\sin(\phi) \\ -(W-B)\cos(\theta)\cos(\phi) \\ -(y_g W - y_b B)\cos(\theta)\cos(\phi) + (z_g W - z_b B)\cos(\theta)\sin(\phi) \\ (z_g W - z_b B)\sin(\theta) + (x_g W - x_b B)\cos(\theta)\cos(\phi) \\ -(x_g W - x_b B)\cos(\theta)\cos(\phi) - (y_g W - y_b B)\sin(\theta) \end{bmatrix} \tag{2.8}$$

[6, p. 72].

2.5.3 Hydrodynamics

Hydrodynamic Added Mass

A marine vehicle must displace the fluid it is passing through in order to move. This displacement of fluid provides the fluid with kinetic energy it otherwise would not have. This energy is dependent on the hydrodynamic added mass matrix $\boldsymbol{M_A}$ which is a 6×6 system inertia matrix of added mass terms. The general representation of $\boldsymbol{M_A}$ can be found in [6, eq. (6.34)]. The hydrodynamic Coriolis-centripetal matrix $\boldsymbol{C_A}$ can then be found by using $\boldsymbol{M_A}$ in Equation (2.6). [6, Chapter 6.3.3]

The hydrodynamic added mass matrix requires many hydrodynamic derivatives and can be cumbersome to find. Therefore, it is common to simplify the added system inertia matrix by using simplifications based on the vehicle's symmetry. For applications in underwater vehicles where the vehicle has three planes of symmetry and primarily operates at low velocities the following representations of $\boldsymbol{M_A}$ and $\boldsymbol{C_A}$ can be used. [6, Example 6.2 & Chapter 8.1.4]

$$\boldsymbol{M_A} = \boldsymbol{M_A^T} = -\mathrm{diag}(X_{\dot{u}}, Y_{\dot{v}}, Z_{\dot{w}}, K_{\dot{p}}, M_{\dot{q}}, N_{\dot{r}}) \tag{2.9}$$

$$\boldsymbol{C_A(\nu_r)} = \boldsymbol{-C_A^T(\nu_r)} = \begin{bmatrix} 0 & 0 & 0 & 0 & -Z_{\dot{w}} w_r & Y_{\dot{v}} v_r \\ 0 & 0 & 0 & Z_{\dot{w}} w_r & 0 & -X_{\dot{u}} u_r \\ 0 & 0 & 0 & -Y_{\dot{v}} v_r & X_{\dot{u}} u_r & 0 \\ 0 & -Z_{\dot{w}} w_r & Y_{\dot{v}} v_r & 0 & -N_{\dot{r}} r & M_{\dot{q}} q \\ Z_{\dot{w}} w_r & 0 & -X_{\dot{u}} u_r & N_{\dot{r}} r & 0 & -K_{\dot{p}} p \\ -Y_{\dot{v}} v_r & X_{\dot{u}} u_r & 0 & -M_{\dot{q}} q & K_{\dot{p}} p & 0 \end{bmatrix}. \tag{2.10}$$

This simplification holds in practice as the diagonal elements in $\boldsymbol{M_A}$ often dominate the off-diagonal elements. For the use case stated above, this simplification reduces the time spent on finding the hydrodynamic derivatives without sacrificing precision. [6, Example 6.2]

Hydrodynamic Damping

Hydrodynamic damping in marine vehicles is caused by several different physical effects, i.e., potential damping, skin friction, wave drift damping, and damping due to vortex shedding. These give both linear and nonlinear damping effects on the vehicle and it can be difficult to distinguish between the effects of different phenomena. Therefore, the total hydrodynamic damping for a marine vehicle is often expressed as:

$$\boldsymbol{D}(\boldsymbol{\nu_r}) = \boldsymbol{D} + \boldsymbol{D_n}(\boldsymbol{\nu_r}) \tag{2.11}$$

where $\boldsymbol{D}$ is the linear damping term caused by and $\boldsymbol{D_n}(\boldsymbol{\nu_r})$ is the nonlinear damping term. [6, pp. 148-149]

For underwater vehicles that operate below the wave-affected zone, the potential damping terms disappear [6, p. 151]. If the vehicle has three planes of symmetry and is performing non-coupled motions, it is also beneficial to assume the diagonal terms in the damping matrices are dominant. This means the damping terms can be expressed as: [6, p. 196]

$$\boldsymbol{D} = -\text{diag}(X_u, Y_v, Z_w, K_p, M_q, N_r) \tag{2.12}$$

$$\boldsymbol{D}(\boldsymbol{\nu_r}) = -\text{diag}(X_{|u|u}|u|, Y_{|v|v}|v|, Z_{|w|w}|w|, K_{|p|p}|p|, M_{|q|q}|q|, N_{|r|r}|r|). \tag{2.13}$$

The hydrodynamic added coefficients, damping terms, restoring terms, and more system coefficients are generally calculated by computer programs using 2D or 3D potential theory, where the commercial program WAMIT is the de facto industry standard in the oil and gas industry [6, Chapter 5.1.1].

2.6 Control Allocation

Note: This section (2.6) is taken directly from the project report [8, Chapter 4.4]. It is included in this thesis as it is relevant and the thesis directly builds on that previous work.

The generalized control forces are $[X, Y, Z, K, M, N]^T$. The generalized control force vector is $\boldsymbol{\tau} \in \mathbb{R}^6$ which is the output vector of the control law. To apply the generalized control forces to a vehicle using the system actuators, a control allocation problem must be solved. This problem can in some cases be solved directly. Alternatively, it can be solved as an optimization problem. For linear systems, the control allocation problem is given as:

$$\boldsymbol{\tau} = \boldsymbol{B}\boldsymbol{u}$$

where $\boldsymbol{B}$ is the input matrix and $\boldsymbol{u} \in \mathbb{R}^r$, where r is the number of actuators on the vehicle. [6]. If $r > n$ the vehicle is overactuated, if $r = n$ the vehicle is fully actuated and

if $r < n$ the vehicle is underactuated. Systems with a square input matrix can be solved as

$$\boldsymbol{u} = \boldsymbol{B}^{-1}\boldsymbol{\tau}.$$

Generally, the control allocation problem is modeled and solved as an optimization problem. [6]

Moore-Penrose Pseudoinverse

For over-actuated control problems or problems where the extended thrust matrix is used, the Moore-Penrose pseudoinverse can be used to solve the control allocation problem. This pseudoinverse is used as the control allocation matrix $\boldsymbol{B}$ is non-square for over-actuated control problems and $\boldsymbol{B}^{-1}$ does not exist. Therefore, $\boldsymbol{B}^{\dagger}$ is used instead. [6]

$$\boldsymbol{B}^{\dagger} = \boldsymbol{B}^{T}(\boldsymbol{B}\boldsymbol{B}^{T})^{-1}$$

2.7 Environmental Disturbances

2.7.1 Ocean Currents

As shown in Equation (2.3) the ocean current forces are included in the model through the relative velocity vector $\boldsymbol{\nu_r}$. This is done by replacing the absolute velocity vector $\boldsymbol{\nu}$ and its derivative $\dot{\boldsymbol{\nu}}$ with the corresponding relative velocity vectors $\boldsymbol{\nu_r}$ and $\dot{\boldsymbol{\nu}}_{\boldsymbol{r}}$ for the hydrodynamic added terms. The rigid body terms remain unchanged. This section defines $\boldsymbol{\nu_c}$ and $\dot{\boldsymbol{\nu}}_{\boldsymbol{c}}$ so that $\boldsymbol{\nu_r} = \boldsymbol{\nu} - \boldsymbol{\nu_c}$ and $\dot{\boldsymbol{\nu}}_{\boldsymbol{r}} = \dot{\boldsymbol{\nu}} - \dot{\boldsymbol{\nu}}_{\boldsymbol{c}}$ can be found. [6, pp. 261-262]

A common assumption is that the ocean current velocity $\boldsymbol{\nu}_{\boldsymbol{c}}^{\boldsymbol{n}}$ in $\{n\}$ is irrotational and constant [6, p. 262]. This means the generalized irrotational velocity vector of the ocean current is:

$$\boldsymbol{\nu_c} = [u_c^b, v_c^b, w_c^b, 0, 0, 0]^T. \tag{2.14}$$

As the angular velocity terms are all zero $\boldsymbol{\nu_c}$ can be simplified to $\boldsymbol{v}_{\boldsymbol{c}}^{\boldsymbol{b}} = [u_c, v_c, w_c]^T$. Using this new definition the ocean current contribution in $\{b\}$ can be defined as:

$$\boldsymbol{v}_{\boldsymbol{c}}^{\boldsymbol{b}} \coloneqq \boldsymbol{R}^{\boldsymbol{T}}(\boldsymbol{\Theta}_{\boldsymbol{nb}})\boldsymbol{v}_{\boldsymbol{c}}^{\boldsymbol{n}}. \tag{2.15}$$

meaning

$$\boldsymbol{\nu_r} = \begin{bmatrix} \boldsymbol{v}^{\boldsymbol{b}} - \boldsymbol{v}_{\boldsymbol{c}}^{\boldsymbol{b}} \\ \boldsymbol{\omega}_{\boldsymbol{nb}}^{\boldsymbol{b}} \end{bmatrix} \tag{2.16}$$

Then, according to [6, Definition 10.1], $\dot{\boldsymbol{v}}_{\boldsymbol{c}}^{\boldsymbol{b}}$ can be defined as:

$$\dot{\boldsymbol{v}}_{\boldsymbol{c}}^{\boldsymbol{b}} \coloneqq -\boldsymbol{S}(\boldsymbol{\omega}_{\boldsymbol{nb}}^{\boldsymbol{b}})\boldsymbol{v}_{\boldsymbol{c}}^{\boldsymbol{b}}. \tag{2.17}$$

The vehicle dynamics, with ocean currents included, can then be simplified and expressed on state space form using the following 6-DOF representation:

$$\begin{aligned} \dot{\boldsymbol{\eta}} &= \boldsymbol{J}_{\boldsymbol{\Theta}}(\boldsymbol{\eta})\boldsymbol{\nu} \\ \dot{\boldsymbol{\nu}} &= \begin{bmatrix} \dot{\boldsymbol{v}}_{\boldsymbol{c}}^{\boldsymbol{b}} \\ \boldsymbol{0}_{\boldsymbol{3\times 1}} \end{bmatrix} + \boldsymbol{M}^{-\boldsymbol{1}}(\boldsymbol{\tau} + \boldsymbol{\tau}_{\boldsymbol{wave}} + \boldsymbol{\tau}_{\boldsymbol{wind}} - \boldsymbol{C}(\boldsymbol{\nu}_{\boldsymbol{r}})\boldsymbol{\nu}_{\boldsymbol{r}} - \boldsymbol{D}(\boldsymbol{\nu}_{\boldsymbol{r}})\boldsymbol{\nu}_{\boldsymbol{r}} - \boldsymbol{g}(\boldsymbol{\eta})) \end{aligned} \tag{2.18}$$

where $\boldsymbol{M} = \boldsymbol{M_{RB}} + \boldsymbol{M_A}$, and $\boldsymbol{C}(\boldsymbol{\nu_r}) = \boldsymbol{C_{RB}}(\boldsymbol{\nu_r}) + \boldsymbol{C_A}(\boldsymbol{\nu_r})$. [6, Chapter 10.3]

2.7.2 Wave Forces

For the purpose of simulating the effect of waves on a vehicle for motion control purposes, the effects of the wave forces are split into two contributions. These forces are expressed by the sum:

$$\boldsymbol{\tau_{wave}} = \boldsymbol{\tau_{wave1}} + \boldsymbol{\tau_{wave2}} \tag{2.19}$$

where $\boldsymbol{\tau_{wave1}}$ are the first-order wave induced forces, and $\boldsymbol{\tau_{wave2}}$ are the second-order wave induced forces [6, Equation 10.40]. These forces are described in [6, p. 274] as:

First-order Wave-induced Forces: "First-order wave-induced forces are the wave-frequency (WF) motion observed as zero-mean oscillatory motions."
and
Second-order Wave-induced Forces: "Second-order wave-induced forces are wave drift forces observed as nonzero slowly-varying components."

As it is undesirable to have oscillatory disturbance components sent through the control feedback loop, the first-order wave-induced forces are generally filtered out using a notch filter. This is due to this component being pure zero-mean oscillations and compensating for these forces can cause unnecessary strain on the control system and actuators. This means only low-frequency second-order wave-induced forces are compensated for by the control system. This allows the vehicle to avoid drifting off course due to wave forces but keeps the WF components out of the control loop. This method of isolating the LF components of the wave forces is called wave filtering. [6, Chapter 13.2]

In order to obtain the wave force components for the purpose of simulation, a couple of methods are generally used. Either the forces are computed through response amplitude operators (RAO) or through linear state-space models (WF models) [6, p. 274]. The RAO methods require hydrodynamic programs to calculate RAO tables as the wave forces depend on the vehicle geometry. Using linear state-space models is a simpler way of calculating the forces, but it can only be used for performance and robustness analysis for control systems. Wave spectra can be used to describe sea-states. These are models that can be used in computer simulations. For this thesis, the JONSWAP spectrum is relevant. This spectrum is used to describe non-fully developed seas. [6, Chapter 10.2]

Chapter 3

Guidance and Navigation Systems

This chapter describes the theory regarding guidance and navigation systems used for motion control in marine vehicles.

Definition 3.1. *"Guidance is the action or the system that continuously computes the reference (desired) position, velocity, and attitude of a marine craft to be used by the motion control system. These data are usually provided to the human operator and the navigation system."* - [6, p. 311]

Guidance systems are algorithms designed to generate a reference for a vehicle to follow that allows it to achieve the motion control objective [6, p. 331]. There are several variations of these kinds of systems allowing for autonomous control in a wide range of operation types. The most notable variations are setpoint regulation, trajectory tracking, target tracking, and path-following [6, pp. 331-332]. For underwater vehicles guidance systems often consists of two subsystems, attitude and path-following systems, generating a reference for several DOF [6, p. 332]. The output of the guidance system is a reference that is sent to the motion control system, realizing the desired control objective [6, p. 311].

Definition 3.2. *"Navigation is the science of directing a craft by determining its position, attitude, course, and distance traveled. In some cases, velocity and acceleration are determined as well."* - [6, p. 311]

Navigation systems are systems that measure a vehicle's position, orientation, velocity, and other desired parameters which then can be used in a guidance system. This is usually done by pairing sensors and state estimators, like Kalman Filters, creating an understanding of the vehicle's current state values for feedback control. Two main navigation systems are used for marine crafts. One being model-based navigation systems and the other being inertial navigation systems. [6, p. 311]

3.1 Path-following LOS Guidance

Path following is one of several guidance methods used to automatically generate a reference for marine crafts. This method is based on controlling the vehicle towards a

pre-defined path independently of time. This means there are no time constraints affecting the vehicle path, only spatial constraints like obstacles or other positional constraints. [6, Chapter 12.4]

One method of realizing a path-following guidance system is by using a line-of-sight (LOS) guidance method. This method can be described as a three-point guidance scheme, where the vehicle, a reference point, and the target destination form a triangle. Using these three points the algorithms create a LOS vector that defines the vehicle's motion towards the target. Three important parameters used in LOS guidance are the lookahead distance (Δ), the cross-track error (y_e^p), and the path-tangential angle (π_p). The definition of these parameters can be seen in Figure 3.1, along with the LOS vector. [6, Chapter 12.2.1]

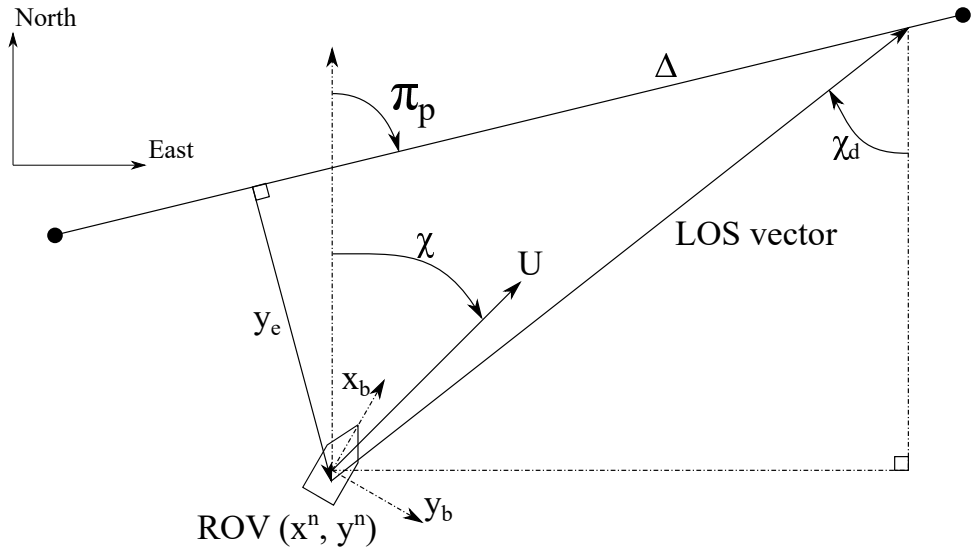

Figure 3.1: Illustration of LOS path-following, Inspired by [6, Figure 12.14]

In some cases, modeling errors or lacking sensor data can cause errors in the course angle (χ). These can be removed by adding an integral term to the LOS guidance algorithm. This method is called integral line-of-sight (ILOS). When using heading autopilots the crab angle (β_c) needs to be compensated for to obtain the desired heading (ψ_d) from the LOS guidance system. This can be done using ILOS. For further reading on path-following guidance systems, the reader is referred to [6, Chapter 12.4-12.6]. [6, Chapter 12.4.4 & 12.5]

3.2 Reference Models

To avoid large discontinuities in the reference sent to a control system a reference model is used. Linear reference models are often used in practical systems due to their simplicity and are commonly made up of low-pass filters or mass-spring-damper systems. Velocity reference models are commonly second-order systems or higher so that smooth references in both the velocity and acceleration are obtained. Position and attitude reference models

are often third-order systems in order to obtain smooth references in position, velocity, and acceleration. [6, Chapter 12.1.1]

A third-order reference model can be made by cascading a mass-spring-damper system with a low-pass filter. The following equations show the transfer function of a third-order reference model and a common expansion of the expression.

$$\frac{x_d}{r} = \frac{\omega_n^2}{(Ts+1)(s^2+2\zeta\omega_n+\omega_n^2)} \tag{3.1}$$

if $T = 1/\omega_n > 0$ the transfer function can be expanded to:

$$\frac{x_d}{r} = \frac{\omega_n^3}{s^3+(2\zeta+1)\omega_n s^2+(2\zeta+1)\omega_n^2 s+\omega_n^3} \tag{3.2}$$

where x_d is the desired state, r is the reference, ζ is the filters relative damping ratio, and ω_n is the filters natural frequency [6, Chapter 12.1.1].

3.3 Discrete Numerical Derivatives

In some cases, it can be useful to be able to find a numerical approximation of a signal's derivative with respect to time. There are several ways of doing this but here two methods are presented. Numerical derivatives are often affected by noisy measurements and should be used with care [6]. The first way of approximating derivatives is by using the definition of the derivative:

Definition 3.3 (**Derivative**)**.**

$$f'(x) = \lim_{h\to\infty} \frac{f(x+h)-f(x)}{h} \tag{3.3}$$

where $f(x)$ is a function, $f'(x)$ is the function derivative. [11, Equation 5.7.1]

This definition can then be altered to give discrete-time derivatives by approximating $h = \Delta t$ and rewriting the equation to:

$$\frac{dx}{dt} \approx \frac{\Delta x}{\Delta t} = \frac{x - x_{previous}}{t - t_{previous}} \tag{3.4}$$

where Δt is the time passed between two measurements and Δx is the difference between the previous and current signal measurements. [11, Chapter 5.7]

Another way of finding the numerical derivative of a signal is by using a technique called filtered differentiation. This method uses a high-pass filter to approximate the derivative of a signal. A basic filter that exhibits this effect is the first-order high-pass filter. This filter can be expressed using the following transfer function:

$$\frac{d\eta}{dt}(s) \approx \frac{Ts}{Ts+1}\eta(s) \tag{3.5}$$

Using the state space formulation of the continuous-time transfer function a discrete-time analytical solution can be found. This model can be used to find a numerical approximation of a time-varying signals (η) derivative and is expressed as:

$$\begin{aligned} x[k+1] &= e^{-\frac{h}{T}}x[k] - (e^{-\frac{h}{T}} - 1)u[k] \\ y[k] &= -x[k] + u[k] \end{aligned} \tag{3.6}$$

where $u = \eta$, $y = \dot{\eta}$, $h = \Delta t$, and T is a user defined constant. Alternatively, the discrete time state space model of Equation (3.5) can be used, solving $\dot{x}[k]$ by using a numerical integrator. [6, Appendix B.3]

Chapter 4

Control Systems

4.1 PID Controllers

Propotional-integral-derivative (PID) controllers are a widely used set of standard controllers. This controller type consists of three parts which can be tuned to obtain satisfactory system performance. PID controllers are a well-known, high-performing, and customizable control method which makes them a common choice in control design. Table 4.1 shows the standard PID control law and some common variations, here $\tilde{x} = x - x_d$ where x_d is the desired value of x, and K_n where $n \in \{p, i, d\}$ are the controller gains [6, eq. (15.110)]. Further reading on PID controllers, tuning of the PID gain parameters, the different variations of PID controllers, and reference feed-forward can be found in [12, pp. 345-427]. [12, Chapter 9][6, Chapter 15]

Controller:	**Control Law:**
P:	$-K_p\tilde{x}$
PD:	$-K_p\tilde{x} - K_d\dot{\tilde{x}}$
PI:	$-K_p\tilde{x} - K_i\int_{t_0}^{t}\tilde{x}\,dt$
PID:	$-K_p\tilde{x} - K_d\dot{\tilde{x}} - K_i\int_{t_0}^{t}\tilde{x}\,dt$

Table 4.1: Standard PID Variations

There are several ways of implementing, designing, and tuning PID. Some examples are successive loop closure, feed-forward disturbance compensation, and pole-placement algorithms. These methods are state-of-the-art PID methods used to improve the performance of PID controllers in complex dynamical systems. These topics are covered in [6, pp. 493-548] and [13]. [6, Chapter 15]

4.2 Sliding Mode Controllers

SMC is a type of nonlinear control that is robust to parametric uncertainties and unmodeled dynamics. This type of control obtains its robust characteristic by utilizing a

discontinuous control signal where the controller can choose from several continuous control structures based on the system's current state space position. [6, p. 634]

SMC makes use of a sliding surface, defined as $S \coloneqq \{\tilde{x} : \sigma(\tilde{x}) = 0\}$, where the dynamics of the system are known [6, eq. (16.443)]. A visualization of the sliding surface can be seen in Figure 4.1. Sliding mode occurs when the system state reaches $\sigma(\tilde{x}(t)) = 0$ and stays there for all future values of t. When the system is in sliding mode the dynamics are known and are defined by the sliding variable σ. It is common to choose a sliding variable so that the system dynamics during sliding mode are exponentially stable. The system dynamics being exponentially stable during sliding mode implies that after defining a sliding variable the control design objective becomes ensuring that the system reaches the sliding surface in finite time. This can be done by analyzing the system using Lyapunov stability theory and designing a nonlinear term in u ensuring that the equilibrium, $\sigma = 0$, is globally asymptotically stable (GAS). [6, Chapter 16.4]

The main issue with conventional SMC is that the control law requires a $K_\sigma sgn(\sigma)$ term to obtain stability. This term can cause chattering, especially for large values of K_σ. Chattering can cause strain on the vehicle's actuators and is not something desired in the controller response. Therefore, $sgn(\sigma)$ is often substituted by Equation (4.1) or by $\tanh(\sigma/\phi)$, where $\phi > 0$ is a design parameter, to remove the discontinuity in the control law caused by $sgn(\sigma)$. These substitutions remove the chattering effect but have the downside of reducing the controller robustness. [6, Chapter 16.4.1]

$$sat(\sigma) = \begin{cases} sgn(\sigma) & if|\sigma/\phi| > 1 \\ \sigma/\phi & otherwise \end{cases} \tag{4.1}$$

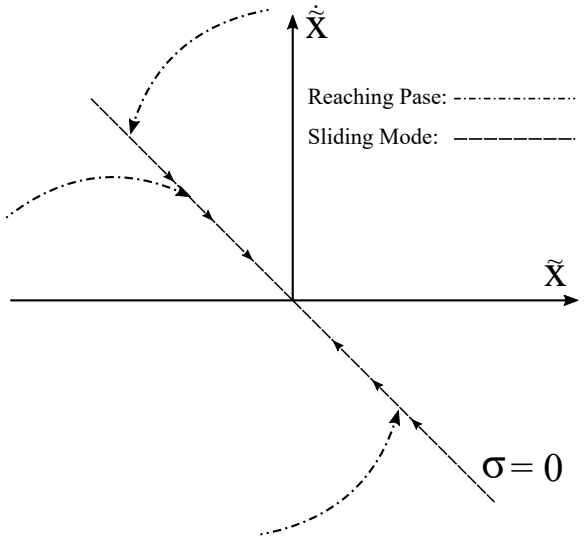

Figure 4.1: Visualization of a Sliding Surface, Inspired by [6, Figure 16.25]

4.3 Higher Order Sliding Mode Control

One way of reducing the chattering effect in SMC without sacrificing any robustness is by using a HOSM technique. These techniques control both the sliding variable (σ) and the sliding variables derivative ($\dot{\sigma}$) to zero. Of the second-order HOSM techniques the super-twisting algorithm (STA) is among the best performing ones [14]. The STA avoids the chattering issue by moving the discontinuous elements of the control signal behind an integrator. [5, Chapter 1]

When designing a STA controller a suitable sliding variable must be selected. A general rule for selecting the sliding variable for marine control applications is

$$\sigma \coloneqq x^{(n-1)} - x_r^{(n-1)} \tag{4.2}$$

where

$$(n = 2) \quad \dot{x}_r = \dot{x}_d - \lambda\tilde{x} \tag{4.3}$$

$$(n = 3) \quad \ddot{x}_r = \ddot{x}_d - 2\lambda\dot{\tilde{x}} - \lambda^2\tilde{x}, \tag{4.4}$$

$\lambda > 0$ is a design parameter for the controller bandwidth, and n is defined by the nonlinear model

$$x^{(n)} = f(\boldsymbol{x}, t) + \gamma(\boldsymbol{x}, t)u + d \tag{4.5}$$

where $\boldsymbol{x} = [x, \dot{x}, ..., x^{(n-1)}]^T \in \mathbb{R}$, $u \in \mathbb{R}$ is the control input, and d is some bounded disturbance. [6, Chapter 16.4.3]

The GSTA is one of several STA variations and can be expressed as

$$u = -k_1\phi_1(x) + z \tag{4.6}$$

$$\dot{z} = -k_2\phi_2(x) \tag{4.7}$$

where

$$\phi_1(x) = \lceil x \rfloor^{\frac{1}{2}} + \beta x \tag{4.8}$$

$$\phi_2(x) = \frac{1}{2}\lceil x \rfloor^0 + \frac{3}{2}\beta\lceil x \rfloor^{\frac{1}{2}} + \beta^2 x, \tag{4.9}$$

x is the system state, k_1, k_2 and β are the controller gains, and $\lceil a \rfloor^b = |a|^b sgn(a)$ [15, eq. (5)]. The GSTA has the benefit of having proven stability for systems where both the perturbations and the control coefficients are uncertain and depend on time. Other STA convergence conditions were found using conservative assumptions, the GSTA was created as a general case STA avoiding this. [5][15]

Theorem A.1 gives the range of the controller gains, k_1 and k_2, which make the system globally finite-time stable. The downside of this method is that Theorem A.1 requires an estimate of the bounds on the perturbations and the control coefficients. The gain $\beta > 0$ can be chosen freely by the designer. The terms in $\phi_1(x)$ and $\phi_2(x)$ related to β help

guarantee the equilibrium's global stability. β can be tuned to reduce the effect of state-dependent perturbations acting on the system, by making its value large. Additionally, a large value of β can help reduce the minimum values of k_1 and k_2, reducing any potential chattering effect the system might exhibit. [15]

An alternative to using fixed gain values for k_1 and k_2 is to use an adaption law. The following is an adaption law was created for the GSTA.

$$\dot{k}_1 = \begin{cases} \omega\sqrt{\frac{\gamma}{2}} & if \sigma \neq 0 \\ 0 & otherwise \end{cases} \tag{4.10}$$

$$k_2 = 2\varepsilon k_1 + \lambda + 4\varepsilon^2 \tag{4.11}$$

where $\varepsilon \in \mathbb{R}$, $\lambda \in \mathbb{R}$, $\gamma \in \mathbb{R}$, and $\omega \in \mathbb{R}$ are positive constants [5, pp. 4-5]. The benefit of the adaption law is that it is able to keep the system in sliding mode by updating the gains. Additionally, this method does not require an estimate of the upper bound on the system perturbations. The perturbation bound only needs to exist for the adaption law to be stable. Theorem A.2 shows the requirements for the system to be proven globally finite-time stable. [5]

Chapter 5

Previous Work

SINTEF and NTNU have had several research projects and master theses working towards robust autonomous control of subsea vehicles in exposed aquaculture fish farms. These projects resulted in relevant models and algorithms that this thesis can build upon. This section presents the relevant previous work done which will be verified and built upon in this project.

5.1 FhSim Simulation Objects

Previous SINTEF research projects on marine systems have provided several useful simulation objects in FhSim. Examples of such objects are ROV models, algorithms simulating environmental forces, aquaculture net structures, sensor models, guidance systems, state estimators, and more. The relevant simulation objects and their function with respect to this project will be described Section 6.2 when they are used to create the desired simulation environment for this thesis.

5.2 Navigation and Guidance Algorithms

In [10] the author presents a method of calculating the position and velocities of an ROV relative to a net-pen by using measurements from a doppler velocity log (DVL), and an ILOS guidance system able to navigate around aquaculture net pens autonomously. These methods were implemented into FhSim during that project and are meant to be used for autonomous tracking of net pens using the ARGUS Mini ROV. Therefore, there is potential to use these programs, with minimal changes, in this thesis to simulate net inspection operations at an aquaculture fishery.

5.2.1 DVL Navigation System

A part of the sensory system on the ARGUS Mini ROV is a DVL. This sensor is used for both obtaining the relative velocities of the ROV with respect to the net-pen and to find the desired heading value and current crosstrack error which is used in the guidance

system.

The velocity measurements from a DVL expressed in $\{b\}$ ($\boldsymbol{v^b_{d/n}}$) is

$$\boldsymbol{v^b_{d/n}} = [u, v, 0]^T + [0, 0, r]^T \times \boldsymbol{r^b_{b/dvl}} + \boldsymbol{R^b_d(\Theta_{db})w^d_{dvl}} \tag{5.1}$$

where $\boldsymbol{r^b_{b/dvl}}$ is the relative position vector of the DVL in $\{b\}$, $\boldsymbol{R^b_d(\Theta_{db})}$ is the relative orientation of the DVL in $\{b\}$ expressed as a rotation matrix, and $\boldsymbol{w^d_{dvl}}$ is the sensor measurement noise [10, eq. (8)].

Using the DVL measurements an approximation of the net pen can be created. This is done by using 3 or more of the received DVL beams to approximate a plane where the net pen is. The normal angle to the plane in $\{n\}$ (ψ_d) and the ROV distance from the plane ($d_{b/net}$) can then be expressed as

$$\psi_d \coloneqq atan2(y^n_{projection}, x^n_{projection}) \tag{5.2}$$

where $x^n_{projection}$ and $y^n_{projection}$ are the x- and y-components of a projection of the approximated planes normal vector to the north-east plane [10, p. 6].

$$d_{b/net} \coloneqq |\boldsymbol{(v^d)^T n^d_{unit}}| \tag{5.3}$$

where $\boldsymbol{v^d}$ is the vector from the CO to where the x-axis of the DVL coordinate frame $\{d\}$ intersects the approximated plane, and $\boldsymbol{n^d_{unit}}$ is the unit normal vector to the approximated plane [10, p. 6]. For the complete explanation of Equation (5.2) and Equation (5.3) the reader is referred to [10, pp. 5-6]. [10]

5.2.2 ILOS Course Guidance

The guidance law presented is based on ILOS and follows a desired course vector around the net-pen. As the Argus Mini ROV is over-actuated it is able to move freely in the north-east plane without relying on a specific heading angle. This is exploited in the guidance algorithm, allowing for the output to be desired surge- (u_d) and sway (v_d) velocities without the need to control the heading angle (ψ). This implies that the guidance algorithm is only valid for vehicles fully actuated in the north-east plane [10, p. 7]. This gives the operator the freedom of selecting the heading angle, which can be beneficial when doing net-inspection operations. [10]

The guidance law can be expressed by

$$\chi_{LOS} = \pi_p - \arctan(\frac{y_e}{\Delta}) \tag{5.4}$$

where $\pi_p = \psi_d \pm \pi/2$, $y_e = d_{b/net} - d_{desired}$, $d_{desired}$ is the desired ROV following distance from the net, and Δ is the lookahead distance [10, eq. (26)].

$$\begin{aligned} u_d &\coloneqq U_d \cos(-\psi + \chi_{LOS}) \\ v_d &\coloneqq U_d \sin(-\psi + \chi_{LOS}) \end{aligned} \tag{5.5}$$

where U_d is the desired total ROV velocity [10, eq. (27)]. [10, Section 4]

5.3 FhSim

FhSim is a software framework, developed at SINTEF Ocean, capable of simulating and visualizing the dynamics of a system. It was developed as a generic framework able to simulate marine environments and systems using mathematical models based expressed as ordinary differential equations. The development of FhSim was motivated by there not being a generic framework allowing simple and efficient re-use of programs from previous projects. This meant projects were often tailored for a specific use case, and not made to be re-used in future projects. FhSim solves this project by having a set of rules and standards all projects must abide by, ensuring the compatibility of all software developed within the framework. [16, p. 1]

FhSim uses numerical solvers to find the time domain solutions of the implemented models. The numerical methods supported by FhSim are Eulers methods, Heun's method and Runge Kutta methods. The solver can use both adaptive and fixed timesteps. For fixed timesteps, the user must make sure that the timestep is dimensioned to fulfill the criteria for simulation time, numerical error tolerances, and obtain numerical stability. The adaptive timestep option chooses a fitting timestep by utilizing an algorithm for error estimation, ensuring the solution error for the current timestep is within the specified tolerance. [16, p. 5]

The software framework is built up of a few key components. These components and the structure they have can be seen in Figure 5.1. Here FhSim is the main component in the structure, connecting the information passed from the subcomponents [16, p. 3]. The reader is referred to [16] for more information on the specifics of each component and FhSim's structure, and [17] for examples of functionality and design principles using FhSim.

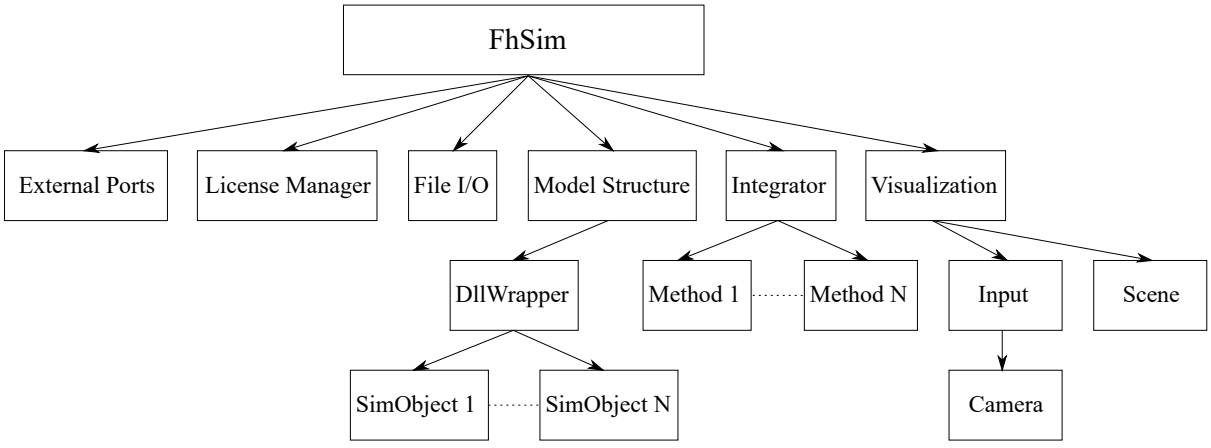

Figure 5.1: FhSim Structure With Visualization, Recreated from [18, Figure 1.2]

Part III

Method

Chapter 6

Simulation Models

Two different simulation models were used in this thesis. A 4-DOF simplified model implemented in MATLAB and a 6-DOF complete process plant model in FhSim. The MATLAB model is developed specifically for this thesis and is used for initial tests of the control laws before implementing them into FhSim. This is beneficial as programming in MATLAB is more streamline and less time-consuming than programming in C++. Potential control design issues could be easily identified in MATLAB before further implementations into FhSim, making fault detection simple and streamlining the development process. Another benefit of MATLAB is the simplicity of changing model and controller parameters. This makes the initial tuning of the controller gains efficient. Once acceptable controller gains are found the user can verify and fine-tune them on the detailed process plant in FhSim. All simulations presented as results in this thesis are done on the detailed FhSim process plant model. Any controllers or guidance algorithms scheduled for a real-world test should first prove their stability on the FhSim plant.

6.1 4-DOF MATLAB Model

The 4-DOF model is a reduction of the 6-DOF model presented in Equation (2.1) and Equation (2.3). To reduce the model to 4-DOF it is assumed that the vehicle is passively stable in roll and pitch, and that these DOF are approximately zero. This justifies ignoring the roll (ϕ) and pitch (θ) DOF. Since roll and pitch are approximately zero, it means the rotation matrix $\boldsymbol{J_\Theta(\eta)}$ can be approximated by $\boldsymbol{J_\Theta(\psi)}$ and $\boldsymbol{g(\eta)}$ can be approximated by $\boldsymbol{g}$. These substitutions can be found by inserting the assumption of zero roll (ϕ) and pitch (θ), then calculating the result.

It is then assumed that the CO of $\{b\}$ and CG coincide, and that the CG and the CB are aligned on the same vertical axis in $\{b\}$, meaning $\boldsymbol{r_{bg}^b} = \boldsymbol{0_{3\times1}}$ and $\boldsymbol{r_{bg}^b} = [0, 0, z_b]^T$. These assumptions are used to further simplify the hydrostatic matrix, as this term is affected by both $\boldsymbol{r_{bb}^b}$ and $\boldsymbol{r_{bg}^b}$. The resulting rotation and hydrostatic matrices can then

be expressed as:

$$\boldsymbol{J_\Theta(\psi)} = \begin{bmatrix} \cos(\psi) & -\sin(\psi) & 0 & 0 \\ \sin(\psi) & \cos(\psi) & 0 & 0 \\ 0 & 0 & 1 & 0 \\ 0 & 0 & 0 & 1 \end{bmatrix}$$

$$\boldsymbol{g} = \begin{bmatrix} (W-B)\sin(\theta) \\ -(W-B)\cos(\theta)\sin(\phi) \\ -(W-B)\cos(\theta)\cos(\phi) \\ -(x_gW - x_bB)\cos(\theta)\cos(\phi) - (y_gW - y_bB)\sin(\theta) \end{bmatrix} = \begin{bmatrix} 0 \\ 0 \\ -(W-B) \\ 0 \end{bmatrix}.$$

The Argus Mini is a box shaped vehicle and is therefore assumed to to have three planes of symmetry. This assumption makes it possible to approximate the damping matrices and the mass matrices as diagonal matrices. The validity of this approximation is presented in Section 2.5.3. This results in the following parameter matrices for mass and damping:

$$\boldsymbol{M_{RB}} = diag(m, m, m, I_z^{CG}), \qquad \boldsymbol{M_A} = -diag(X_{\dot{u}}, Y_{\dot{v}}, Z_{\dot{w}}, N_{\dot{r}})$$
$$\boldsymbol{D(\nu_r) = D + D_{nl}(\nu_r)}, \qquad \boldsymbol{D} = -diag(X_u, Y_v, Z_w, N_r)$$
$$\boldsymbol{D_{nl}(\nu_r)} = -diag(X_{|u|u}|u|, Y_{|v|v}|v|, Z_{|w|w}|w|, N_{|r|r}|r|)$$

The Lagrangian parameterization (Equation (2.6)) presents a 6-DOF expression for C_{RB}. The assumption that CG is in CO means that $\boldsymbol{r_{bg}^b = 0_{3\times 1}}$. This simplifies the Lagrangian parametrization of the Coriolis effect to the following matrix:

$$\boldsymbol{C_{RB}(\nu)} = \begin{bmatrix} \boldsymbol{0_{3\times 3}} & -m\boldsymbol{S(\nu_1)} \\ -m\boldsymbol{S(\nu_1)} & -\boldsymbol{S(I_b^b \nu_2)} \end{bmatrix}$$

Then assuming that roll and pitch are stable DOF the expression can be reduced to a 4-DOF matrix by removing the equations and terms associated with roll and pitch. $\boldsymbol{C_{RB}}$ then becomes:

$$\boldsymbol{C_{RB}(\nu)} = \begin{bmatrix} 0 & 0 & 0 & mv \\ 0 & 0 & 0 & -mu \\ 0 & 0 & 0 & 0 \\ -mv & mu & 0 & 0 \end{bmatrix}$$

The 6-DOF representation of $\boldsymbol{C_A}$ is given in Equation (2.10). The 4-DOF representation of $\boldsymbol{C_A}$ is found by removing the terms related to roll and pitch from Equation (2.10), resulting in:

$$\boldsymbol{C_A(\nu_r)} = \begin{bmatrix} 0 & 0 & 0 & Y_{\dot{v}} v_r \\ 0 & 0 & 0 & -X_{\dot{u}} u_r \\ 0 & 0 & 0 & 0 \\ -Y_{\dot{v}} v_r & X_{\dot{u}} u_r & 0 & 0 \end{bmatrix}$$

Finally, the external forces and moments are included. As this model is designed for preliminary testing and is meant to be simple all external forces except for the ocean current are set to 0. Additionally, the ROV is assumed to be fully submerged in water under operations. This means $\boldsymbol{\tau_{wind}}$ and $\boldsymbol{\tau_{wave}}$ can be removed from the kinetic equation

(Equation (2.3)). Using the definitions in Section 2.7.1 the ocean current can be included in model dynamics through the relative velocity vector $\boldsymbol{\nu_r}$. This vector is defined as:

$$\boldsymbol{\nu_r} = \begin{bmatrix} \boldsymbol{v^b} - \boldsymbol{v_c^b} \\ \omega^b_{nb,(3,1)} \end{bmatrix} \tag{6.1}$$

where $\boldsymbol{v^b} = [u, v, w]^T$, $\boldsymbol{v_c^b} = \boldsymbol{R^T(\psi)v_c^n}$, $\boldsymbol{v_c^n} = [V_x, V_y, V_z]^T$ is a user defined irrotatinal current contribution in $\{n\}$, and $\omega^b_{nb,(3,1)} = r$. Keep in mind that p and q are emitted from $\boldsymbol{\omega^b_{nb}}$ to create $\omega^b_{nb,(3,1)}$ because the system is reduced to 4-DOF. Finally, Equation (2.17) can be used to find $\boldsymbol{\dot{v}_c^b}$:

$$\boldsymbol{\dot{v}_c^b} = -\boldsymbol{S(\omega^b_{nb})v_c^b} \tag{6.2}$$

where $\boldsymbol{\omega^b_{nb}} = [0, 0, r]^T$, and $\boldsymbol{S(\omega^b_{nb})}$ is a skew-symmetric matrix.

The final 4-DOF system dynamics can then be fully expressed by Equation (6.3). For this project finding the individual parameters is not necessary, as the relevant 6-DOF parameters presented in Chapter 8.1.1 can be used in this model.

$$\begin{aligned} \boldsymbol{\dot{\eta}} &= \boldsymbol{J_\Theta(\psi)\nu} \\ \boldsymbol{\dot{\nu}} &= \begin{bmatrix} \boldsymbol{\dot{v}_c^b} \\ 0_{1\times 1} \end{bmatrix} + \boldsymbol{M^{-1}}(\boldsymbol{\tau} - \boldsymbol{C(\nu_r)\nu_r} - \boldsymbol{D(\nu_r)\nu_r} - \boldsymbol{g(\eta)}) \end{aligned} \tag{6.3}$$

Here $\boldsymbol{M} = \boldsymbol{M_{RB}} + \boldsymbol{M_A}$, and $\boldsymbol{C(\nu_r)} = \boldsymbol{C_{RB}(\nu_r)} + \boldsymbol{C_A(\nu_r)}$.

6.2 6-DOF FhSim Model

The 6-DOF process plant is made up of several simulation objects created during previous research projects in FhSim. The purpose of this process plant is to be a high-fidelity model that can accurately simulate and validate the developed controllers' performances. All controllers and systems developed should have acceptable performance in this model before being tested on a physical ROV in a real aquaculture fish farm.

The main part of the simulation model is a 6-DOF ROV model created by researchers at SINTEF Ocean. The model code is closed source, but the assumptions and literature the model is based on are presented in Appendix B. In addition to the base model, slew-rate limiters and saturation limits on the thrusters are included to make the ROV thrust response realistic. Together with this simulation model an environmental model, based on the JONSWAP spectrum, is able to model ocean currents and wave forces which can be used in the 6-DOF ROV model. This makes it possible to simulate performance in varying sea states. Finally, aquaculture net pen models are available allowing for the use of the DVL and guidance systems presented in Chapter 5.2. All these simulation objects combined form an accurate simulation environment able to test and verify the control systems developed later in this project. All systems scheduled for a field test should be tested on the FhSim model first so that they are validated beforehand. This reduces the risk of excessive debugging or system failure during a field test.

6.3 Argus Mini ROV

The ROV used in this project is the Argus Mini ROV. This ROV is the one SINTEF Ocean has been using for research in aquaculture fish farms and is therefore used in this thesis. The parameters for the Argus Mini ROV are presented in Section 8.1.1 as a part of the simulation model setup. They were provided by SINTEF Ocean specifically for use in this thesis. These parameters will be used in both models presented in this chapter. The ROV is over actuated and is able to move freely in surge, sway, heave, and yaw.

The ROV has limited sensor data, which is important to note when designing control systems for it. It is able to measure velocities relative to other objects using a DVL. It can measure the heading angle and the heading angle rate using a magneto compass. Finally, it is able to measure its position using a USBL.

Chapter 7

Controller Design

7.1 GSTA Controllers

This chapter presents the development and implementation of different GSTA controllers with and without adaptive gains. The choice of a higher-order SMC was made as they are more robust against the chattering issue conventional SMC experiences. This is beneficial, as robustness is a key property sought after in this thesis. It was decided to design a GSTA controller as this controller type is robust against unmodeled dynamics and disturbances and this specific algorithm has not previously been tested for this use case.

7.1.1 Defining the Sliding Variables

The GSTA defines a control law using some state x. From here on out x will be substituted by the sliding variable σ. The sliding variable defines the dynamics of the system while it is in the equilibrium $\sigma = 0$, also called the sliding plane/sliding mode. Using the general case sliding variable presented in Equation (4.2) as inspiration two sliding variables are defined:

$$\sigma_1 = \tilde{x} + \dot{\tilde{x}} \tag{7.1a}$$

$$\sigma_2 = \tilde{x} + 2\dot{\tilde{x}} + \ddot{\tilde{x}} \tag{7.1b}$$

where $\tilde{x} = x - x_d$, x is the measured state value, x_d is the desired state value and $\lambda = 1$. When deciding the sliding variable the most important factor is that the system is of relative degree one. This allows the system to be restructured on the form $\dot{\sigma} = \varphi(\sigma, t) + \gamma(\sigma, t)u$ which will later be used to prove stability for the controllers. Which sliding variable is used in which controller was found through testing. This choice is further discussed in Chapter 10.3.

For controllers that work with angles the sliding variables are defined as:

$$\sigma = ssa(\tilde{x}) + \dot{\tilde{x}} \tag{7.2a}$$

$$\sigma = ssa(\tilde{x}) + 2\dot{\tilde{x}} + \ddot{\tilde{x}} \tag{7.2b}$$

The $ssa(\cdot)$ function makes sure the controller always makes the shortest rotation in order to reach the reference, avoiding situations where the vehicle performs rotations lager than $\pi[rad]$.

7.1.2 Defining the Control Laws

Controllers for surge, sway, heave, and heading are required for accurate three-dimensional control of the ROV. This allows the ROV to move freely in $\{n\}$, and simultaneously control the heading angle. From here on the heave controller will be referred to as the depth controller. Tilt control is not considered as roll and pitch are assumed stable for the ROV in question, making control in these DOF unnecessary for this project's use case. The control laws are then defined as:

$$\tau = -k_1\phi_1(\sigma) + z$$
$$\dot{z} = -k_2\phi_2(\sigma)$$

where

$$\phi_1(\sigma) = \lceil\sigma\rfloor^{\frac{1}{2}} + \beta\sigma$$
$$\phi_2(\sigma) = \frac{1}{2}\lceil\sigma\rfloor^0 + \frac{3}{2}\beta\lceil\sigma\rfloor^{\frac{1}{2}} + \beta^2\sigma$$

where τ is the one-dimensional controller output, and k_1, k_2 and β are the controller gains. These equations define the control law for all the GSTA controllers. The only variation between the different controllers is the sliding variable and the controller gains. The velocity controllers use Equation (7.1a), the the depth controller uses Equation (7.1b), and the heading controller uses Equation (7.2a) as their respective sliding variables.

Choosing a heading controller instead of a course controller is natural when considering station-keeping operations. This is because the craft velocity vector U is undefined if the vehicle stops moving. In the use case for this thesis, the ROV will be performing low velocity and station-keeping maneuvers, meaning course control of this vehicle is not a viable option. Therefore, a heading controller was chosen.

7.1.3 Selecting the Controller Gains

This project explores both fixed gain and adaptive gain options for the controllers. The fixed gain method requires the developer to find appropriate gains. Theorem A.1 states for which region of gains the controller is globally finite-time stable. This theorem is used to prove the controller stability, then the gains are fine tuned within the stable region. This method can be cumbersome, as it may require a large amount of simulations to find acceptable gains. In order to reduce the amounts of time spent tuning the controllers the MATLAB simulation model is used. This model allows for quick parameter changes and plotting, which is beneficial when running several tests in rapid succession. Once acceptable gains are found using the MATLAB model these gains were imported to the FhSim model and fine tuned.

The adaptive method utilizes the following adaption law to automatically find appropriate controller gains:

$$\dot{k}_1 = \begin{cases} \omega\sqrt{\frac{\gamma}{2}} & if \sigma \neq 0 \\ 0 & otherwise \end{cases}$$

$$k_2 = 2\varepsilon k_1 + \lambda + 4\varepsilon^2$$

where ω, γ, λ, and ε are all positive user-defined gains. The benefit of this adaption law is that it has strong theoretical stability properties as is able to keep the system in sliding mode by updating its gains automatically. The main difference between the fixed-gain and adaptive gain versions is that for the adaptive version the bound on the systems perturbation term only needs to exist and does not need to be known to prove stability, unlike in Theorem A.1 for the fixed-gain variant. This could lead to better controller gains if the adaption law itself is properly tuned. This adaption GSTA method, presented in [5], was recently developed and has never previously been used on an ROV.

7.1.4 Summary/Summary of the Control Law

To summarize, four controllers based on the GSTA were made. These controllers were surge and sway velocity controllers, a depth controller, and a heading controller. The controllers' sliding variables were defined as:

$$\begin{aligned} \sigma_u &= \tilde{u} + \dot{\tilde{u}} && (Surge) \\ \sigma_v &= \tilde{v} + \dot{\tilde{v}} && (Sway) \\ \sigma_\psi &= ssa(\tilde{\psi}) + \tilde{r} && (Heading) \\ \sigma_z &= \tilde{z}^n + 2\tilde{w} + \dot{\tilde{w}} && (Depth) \end{aligned}$$

The gains for the controllers were either fixed gains, or adaptive gains using Equations (4.10)-(4.11) as an adaption law. This means in total four fixed gain GSTA controllers and four adaptive-gain GSTA controllers were created. The final control laws can then be expressed as:

$$\begin{aligned} \tau_i &= -k_1\phi_1(\sigma_i) + z \\ \dot{z} &= -k_2\phi_2(\sigma_i) \end{aligned}$$

and

$$\begin{aligned} \phi_1(\sigma_i) &= \lceil \sigma_i \rfloor^{\frac{1}{2}} + \beta\sigma_i \\ \phi_2(\sigma_i) &= \frac{1}{2}\lceil \sigma_i \rfloor^0 + \frac{3}{2}\beta\lceil \sigma_i \rfloor^{\frac{1}{2}} + \beta^2\sigma_i \end{aligned}$$

where $i \in \{u, v, \psi, z\}$, and $\beta > 0$ is a user defined controller gain. Two versions of each controller were created. One fixed gain version and one adaptive gain version. For the fixed gain GSTA version k_1 and k_2 are user defined constants. For the adaptive gain GSTA version k_1 and k_2 are found through the following adaption law:

$$\dot{k}_1 = \begin{cases} \omega\sqrt{\frac{\gamma}{2}} & if \sigma_i \neq 0 \\ 0 & otherwise \end{cases}$$

$$k_2 = 2\varepsilon k_1 + \lambda + 4\varepsilon^2$$

where ω, γ, λ, and ε all are positive constants defined by the user. The result is eight controllers, split into two different GSTA based control strategies, able to track references in their respective DOF.

7.2 Stability Analysis of the Controllers

This section analyzes the developed controllers' theoretical stability properties using a 4-DOF control plant model of the ROV. The control plant is chosen as:

$$\begin{aligned} \dot{\boldsymbol{\eta}} &= \boldsymbol{J}_{\boldsymbol{\Theta}}(\boldsymbol{\psi})\boldsymbol{\nu} \\ \boldsymbol{M}\dot{\boldsymbol{\nu}} + \boldsymbol{C}(\boldsymbol{\nu})\boldsymbol{\nu} + \boldsymbol{D}(\boldsymbol{\nu})\boldsymbol{\nu} + \boldsymbol{g} &= \boldsymbol{\tau} + \boldsymbol{w}. \end{aligned} \tag{7.3}$$

This is a simplified version of the dynamics where all unmodeled effects are assumed to be external disturbances on the system and are included in the disturbance vector $\boldsymbol{w} \in \mathbb{R}^4$. The purpose of this model is to show that the controllers make the dynamics of the ROV converge to the defined equilibrium.

As the GSTA controllers are one-dimensional the stability proofs will handle one dimension at a time. To assess the stability, the control plant model is split into the following equations:

$$\begin{aligned} \dot{x}^n &= \cos(\psi)u - \sin(\psi)v, \\ \dot{y}^n &= \sin(\psi)u + \cos(\psi)v, \\ \dot{z}^n &= w, \\ \dot{\psi} &= r, \\ (m - X_{\dot{u}})\dot{u} + (mv + Y_{\dot{v}}v)r + (-X_u - X_{|u|u}|u|)u &= \tau_u + w_1, \\ (m - Y_{\dot{v}})\dot{v} + (-mu + X_{\dot{u}}u)r + (-Y_v - Y_{|v|v}|v|)v &= \tau_v + w_2, \\ (m - Z_{\dot{w}})\dot{w} + (-Z_w - Z_{|w|w}|w|)w - (W - B) &= \tau_z + w_3, \\ (I_z^{CG} - N_{\dot{r}})\dot{r} + (-mv - Y_{\dot{v}}v)u + (mu + X_{\dot{u}}u)v + (-N_r - N_{|r|r}|r|)r &= \tau_\psi + w_4. \end{aligned} \tag{7.4}$$

These are the dynamics to be used in their respective controller's stability proofs. The following analyses are based on general stability theorems presented in Theorem A.1 and Theorem A.2, and use these theorems combined with Assumptions A.1-A.4 to prove global finite-time stability. The proofs for Theorem A.1 and Theorem A.2 are found in [15] and [5] respectively.

7.2.1 Heading Controller

The sliding variable for the heading controller is defined as:

$$\sigma_\psi = ssa(\tilde{\psi}) + \tilde{r}. \tag{7.5}$$

For the stability analysis the $ssa(\cdot)$ is removed for simplicity. By using that $r_r = r_d - \tilde{\psi}$ and that $\tilde{r} = r - r_d$, it follows that expression 7.5 can be written as:

$$\sigma_\psi = \tilde{\psi} + r - r_d = \tilde{\psi} - \tilde{\psi} + r - r_r = r - r_r. \tag{7.6}$$

The sliding variable dynamics can then be expressed as:

$$\dot{\sigma}_\psi = \dot{r} - \dot{r}_r \tag{7.7}$$

$$\begin{aligned} \dot{\sigma}_\psi = (I_z^{CG} - N_{\dot{r}})^{-1}(\tau_\psi - (-mv - Y_{\dot{v}}v)u - \\ (mu + X_{\dot{u}}u)v - (-N_r - N_{|r|r}|r|)r) - \dot{r}_r \end{aligned} \tag{7.8}$$

Now, consider the system:

$$\dot{\sigma} = \varphi(\sigma, t) + \gamma(\sigma, t)u \tag{7.9}$$

where $\gamma(\sigma, t)$ is the control coefficient, and $\varphi(\sigma, t)$ is the system perturbation, both uncertain and dependant on state and time, and $u = \tau_\psi$. $\varphi(\sigma_\psi, t) = \varphi_1(\sigma_\psi, t) + \varphi_2(\sigma_\psi, t)$ can be split into two separate functions where $\varphi_1(0, t) = 0$ is the vanishing terms around the equilibrium, and is bounded by $|\varphi_1(\sigma_\psi, t)| \leq \alpha|\varphi_1(\sigma_\psi)|$ in accordance with [15, eq. (8)]. The dynamics that vanish about $\sigma_\psi = 0$ can be found using the definition of the sliding variable $\sigma_\psi = \tilde{\psi} + \tilde{r} \rightarrow r = \sigma_\psi - \tilde{\psi} - r_d$. This results in:

$$\varphi_1(\sigma_\psi, t) = (I_z^{CG} - N_{\dot{r}})^{-1}(-(-N_r - N_{|r|r}|r|)(\sigma_\phi)) \tag{7.10}$$

and

$$\begin{aligned} \varphi_2(\sigma_\psi, t) = (I_z^{CG} - N_{\dot{r}})^{-1}(w_4 - (-mv - Y_{\dot{v}}v)u - \\ (mu + X_{\dot{u}}u)v - (-N_r - N_{|r|r}|r|)(-ssa(\tilde{\psi}) - r_d)) - \dot{r}_r. \end{aligned} \tag{7.11}$$

Then $\gamma(\sigma_\psi, t)$ is found to be:

$$\gamma = (I_z^{CG} - N_{\dot{r}})^{-1} \tag{7.12}$$

rewriting the sliding variable dynamics as $\dot{\sigma}_\psi = \varphi(\sigma_\psi, t) + \gamma\tau_\psi$.

For Theorems A.1 and A.2 to hold Assumptions A.1-A.4 must be true for $\dot{\sigma}_\psi$. Since the dynamics presented are dependent on the velocities of the ROV it is safe to assume they have limited growth with respect to time. Additionally, the reference value is the result of low-pass filtering the guidance algorithm's output avoiding sudden changes in reference. The guidance algorithm is designed to make the ROV follow a path at a constant velocity. Therefore, the reference value and its derivatives can be assumed continuous and bounded. These properties mean that Assumption A.1 holds. As $\gamma = (I_z^{CG} - N_{\dot{r}})^{-1} = M_{RB_\psi} + M_{A_\psi} > 0$ is constant it fulfils Assumption A.2. Finally, as the system has a limited thrust and as it is a mechanical system Assumption A.3 and Assumption A.4 can be assumed to hold as there is a physical bound on the system creating an upper bound on the perturbed state response.

Therefore, as long as the fixed and adaptive gains are designed according to their respective theorems, the equilibrium $\sigma_\psi = 0$ is globally finite time stable following Theorem A.1 for the GSTA and Theorem A.2 for the adaptive GSTA. Additionally, by using the definition of the controllers sliding variable $\sigma_\psi = \tilde{\psi} + \tilde{r}$ the dynamics for $\sigma_\psi = 0$ become $\tilde{r} = -\tilde{\psi} \rightarrow \dot{\tilde{\psi}} = -\tilde{\psi}$ which proves exponential stability while the system is in sliding mode.

7.2.2 Velocity Controllers

As the control plant dynamics and control design of both velocity controllers are nearly identical these are grouped together in the stability proof. The dynamics of the surge model will be used for the analysis, but the results are applicable to the sway velocity controller as well.

The sliding variable used in the surge velocity controllers is:

$$\sigma_u = \tilde{u} + \dot{\tilde{u}}. \tag{7.13}$$

For the velocity controllers $u_r \coloneqq u_d - \dot{\tilde{u}}$. This change is done so that the sliding variable can be expressed as:

$$\sigma_u = u - u_d + \dot{\tilde{u}} = u - u_r - \dot{\tilde{u}} + \dot{\tilde{u}} = u - u_r \tag{7.14}$$

The benefit of this substitution is that it gathers the $\dot{u}$ and velocity reference term in the sliding variable in one term, making for fewer expressions in the upcoming equations. The sliding variable dynamics can now be found as:

$$\dot{\sigma}_u = \dot{u} - \dot{u}_r \tag{7.15}$$

$$\dot{\sigma}_u = (m - X_{\dot{u}})^{-1}(\tau_u + w_1 - (mv + Y_{\dot{v}}v)r - (-X_u - X_{|u|u}|u|)u) - \dot{u}_r. \tag{7.16}$$

Substituting for $u = \sigma_u + u_r$ gives:

$$\begin{aligned}\dot{\sigma}_u = (m - X_{\dot{u}})^{-1}(\tau_u + w_1 - (mv + Y_{\dot{v}}v)r \\ - (-X_u - X_{|u|u}|(\sigma_u + u_r)|)(\sigma_u + u_r)) - \dot{u}_r.\end{aligned} \tag{7.17}$$

Then the standard form $\dot{\sigma} = \varphi(\sigma, t) + \gamma(\sigma, t)$ is introduced. Here:

$$\varphi_1(\sigma_u, t) = (m - X_{\dot{u}})^{-1}(-(-X_u - X_{|u|u}|(\sigma_u + u_r)|)\sigma_u + X_{|u|u}|\sigma_u u_r) \tag{7.18}$$

and

$$\begin{aligned}\varphi_2(\sigma_u, t) = (m - X_{\dot{u}})^{-1}(w_1 - \\ (mv + Y_{\dot{v}}v)r + X_u u_r + X_{|u|u}|u_r|u_r) - \dot{u}_r\end{aligned} \tag{7.19}$$

Finally, $\gamma(\sigma_u, t)$ is found to be:

$$\gamma = (m - X_{\dot{u}})^{-1} = (M_{RB_u} + M_{A_u})^{-1} > 0 \tag{7.20}$$

Following the same logic as in the heading controller proof, the system $\dot{\sigma}_u = \varphi(\sigma_u, t) + \gamma$ is assumed to follow Assumptions A.1-A.4 through that it is a mechanical system, with limited thrust and disturbances, that the reference is bounded and smooth by definition, and that $\gamma > 0$ is a constant. This implied that the equilibrium $\sigma_u = 0$ is globally finite time stable. Additionally, $\sigma_u = 0 = \tilde{u} + \dot{\tilde{u}} \rightarrow \dot{\tilde{u}} = -\tilde{u}$ which is exponentially stable.

7.2.3 Depth Controller

The sliding variable used in the depth controller is:

$$\sigma_z = \tilde{z}^n + 2\tilde{w} + \dot{\tilde{w}} \tag{7.21}$$

For the depth controller $w_r := 2w_d - \tilde{z}^n - \dot{w}$

$$\sigma_z = \tilde{z}^n + 2w - 2w_d + \dot{w} - \dot{w}_d = 2w - w_r. \tag{7.22}$$

Again, this substitution is done to gather some of the higher-order expressions and reference values in one term, reducing the number of expressions in the sliding variable dynamics. The sliding variable dynamics can then be expressed as:

$$\dot{\sigma}_z = 2\dot{w} - \dot{w}_r \tag{7.23}$$

$$\sigma_z = 2(m - Z_{\dot{w}})^{-1}(\tau_z + w_3 - (-Z_w - Z_{|w|w}|w|)w + (W - B)) - \dot{w}_r \tag{7.24}$$

Substituting $w = (1/2)(\sigma_z + w_r)$ gives:

$$\begin{aligned} \sigma_z = 2(m - Z_{\dot{w}})^{-1}(\tau_z + w_3 - \\ (-Z_w - Z_{|w|w}|((1/2)(\sigma_z + w_r))|)((1/2)(\sigma_z + w_r)) + (W - B)) - \dot{w}_r. \end{aligned} \tag{7.25}$$

Introducing the standard form $\dot{\sigma} = \varphi(\sigma, t) + \gamma(\sigma, t)$. $\varphi(\sigma, t)$ can be split into:

$$\begin{aligned} \varphi_1(\sigma_u, t) = 2(m - Z_{\dot{w}})^{-1}(- \\ (-Z_w - Z_{|w|w}|((1/2)(\sigma_z + w_r))|)(1/2)\sigma_z + (1/2)Z_{|w|w}|\sigma_z|w_r) \end{aligned} \tag{7.26}$$

and

$$\begin{aligned} \varphi_2(\sigma_u, t) = (m - Z_{\dot{w}})^{-1}(w_3 + \\ (1/2)Z_w w_r + (1/4)Z_{|w|w}|w_r|w_r - (W - B)) - \dot{w}_r. \end{aligned} \tag{7.27}$$

Then, $\gamma(\sigma_z, t)$ can be found:

$$\gamma = 2(m - Z_{\dot{w}})^{-1} = 2(M_{RB_z} + M_{A_z})^{-1} > 0. \tag{7.28}$$

Finally, following the same reasoning as both previous analyses, Assumptions A.1-A.4 are valid for system $\dot{\sigma_z}$, meaning the equilibrium $\sigma_z = 0$ is globally finite time stable. Then $\dot{\sigma}_z = 0 = \tilde{z}^n + 2\tilde{w} + \dot{\tilde{w}} \rightarrow \dot{\tilde{w}} = -\tilde{z}^n - 2\tilde{w}$ which can be compared to the dynamics of a stable mass-spring-damper system. Therefore, $\sigma_z = 0$ is stable, and the system converges to $\tilde{z}^n = 0$.

7.3 Implementing the Controllers

7.3.1 Numerical Derivatives

The ROV has limited sensors and can therefore not accurately measure all the states required to use the desired sliding variables. For initial performance tests of the controllers, the feedback values can be directly sourced from the process plant. This means the controllers work as intended, as it has all the required feedback data available. This is an ideal simulation and is not representative of the actual controller performance. To make the simulations more representative of real-world performance only the sensor data available on the physical ROV can be used for controller feedback. The ROV is equipped with a magnetic compass, a depth pressure sensor, and a DVL, meaning z, ψ, r, u relative to the aquaculture net pen, and v relative to the aquaculture net pen are the only measurements available for feedback relevant to the control law.

The limited sensor data pose a problem for the controller performance. Not using the sliding variables presented in Section 7.1.1 means reduced controller performance and robustness. To limit the effect of this issue w, $\dot{w}$, $\dot{u}$, and $\dot{v}$ must be approximated.

Two relevant numerical differentiation techniques were presented in Section 3.3. The method using a high-pass filter to approximate the derivatives was chosen as this could use FhSim's integrator directly. This made the filter method preferable, as the function can be made consistent with other implementations in FhSim, utilizes FhSim's strength as a numerical solver, and requires less IO than the alternative method. This was done by designing the filter on a continuous state-space form and integrating the state derivative rather than using the analytical solution presented in Section 3.3. The resulting high-pass filter can then be described by the following state-space representation:

$$\begin{aligned} \dot{x} &= -\frac{1}{T}x + \frac{1}{T}u \\ y &= -x + u \end{aligned} \tag{7.29}$$

where $T > 0$ is the filter's time constant, u is the unfiltered signal, and y is the filter output. This equation is the state space equivalent of the transfer function in Equation (3.5) and is presented in [6]. Finding an appropriate value for T was done experimentally.

7.3.2 Adaption Law Tolerance

Another thing to note when implementing the controllers is that for the adaptive GSTA controllers is that the adaption law requires $\sigma_i = 0$ for $\dot{k}_1 = 0$. In the actual implementation of the system, the value of σ will never exactly be zero due to numerical errors and approximations. Therefore, the adaption law is changed to:

$$\dot{k}_1 = \begin{cases} 0 & if|\sigma| < \alpha_{tol} \\ \omega\sqrt{\frac{\gamma}{2}} & otherwise \end{cases}$$

$$k_2 = 2\varepsilon k_1 + \lambda + 4\varepsilon^2$$

where α_{tol} is some small number working as a tolerance for what is to be considered $\sigma = 0$ in the control law. This alteration was also done in [5] and is a requirement for the adaption law to work.

7.3.3 Reference Models

It is common practice to use a reference model to smooth out the reference signal sent to the controller. This is especially true when using a guidance system, as noisy sensor data can create random spikes in reference. Therefore, third-order reference models are implemented to smooth the output of all references generated by the guidance law. These reference models are defined by Equation (3.2) with the tuning parameters ζ and ω_n.

All reference models have been initialized using the current ROV state value. This is to avoid large gaps between the initial reference and state values in the case of a non-zero ROV state. This avoids potential issues caused by the controller error initially being large, like actuator saturation and integral windup. Additionally, it makes the ROV converge at a rate decided by the reference model, which can be fine-tuned by the designer.

Part IV

Results & Discussion

Chapter 8

Simulation Results

8.1 Simulation Environment

The simulations done in this chapter uses the full process plant model implemented into FhSim. The simulation environment is made to mimic a net following operation at an aquaculture fish farm, where an ROV tracks an aquaculture net pen in the horizontal plane. The method used for net-following is the DVL based ILOS algorithm presented in Section 5.2 which is able to generate a path independent of the heading angle. This is required for operations where for instance the ROV needs to keep a sensor pointing towards the net pen at all times. For these simulations a static approximation is used for the net pen. The following distance (d_d) and the total ROV velocity (U_d) are defined by the operator. This setup allows for testing control systems in scenarios similar to what an ROV would experience in an actual field test. Additionally, all outputs of the guidance model are sent through third-order reference models in order to avoid the reference value spiking. In order to make the simulation environment realistic an environmental model for ocean currents and wave forces are used. This model allows the user to define the ocean current velocity, the ocean current angle, the significant wave height, mean wave period, and wave direction. This environmental model is a simobject previously implemented into FhSim during a different research project. The wave model uses airy wave theory and the JONSWAP spectrum to simulate the wave effects. This means, unlike the MATLAB model, the environmental forces are more accurately included in the simulation. The simulation results are used to analyze the controllers' performances and to verify that the theory presented is valid in simulation.

The simulation setup was made to imitate normal conditions at an exposed aquaculture fish farm found in the Trøndelag region in Norway. This was done as the testing location used for the thesis was the SINTEF ACE full-scale marine laboratory, which is located around Hitra/Frøya off the coast of Trøndelag. Relatively calm conditions were chosen as calm conditions are generally what this ROV operates in. The significant wave height was chosen to be 1 [m]. This value was chosen as the mean significant wave height measured by a wave buoy, over a timeframe of 1.4 years, in the same geographical area is $H_{s,1year} = 1.05$ [m] [19]. Here the subscript 1 year indicates the return period of this significant wave height. Therefore, a simulated significant wave height of 1 [m]

was deemed appropriate. The wave period of 15 [s] was chosen to imitate long waves and calm conditions. Finally, the current was set to 0.6 [m/s] at 0 [rad] and 0.8 [m/s] at 3.1415 [rad]. This choice of ocean current was to make the total ocean current speed 1 [m/s], which according to [2] is around the quickest ocean current experienced at exposed aquaculture locations in Norway. Therefore, the choice of a total current velocity of 1 [m/s] was deemed acceptable for the simulations.

The following simulations will all have the same initial conditions, use the same following distance, desired total velocity, and the same environmental disturbances. These parameters are detailed in the following table.

Simulation Parameters:	
Net Follow Distance (d_d):	3 m
Desired Total Speed (U_d):	0.2 m/s
Significant Wave Height:	1 m
Mean Wave Period:	15 s
Mean Wave Direction:	0 rad
Current Contribution 1:	0.6 m/s @ 0 rad
Current Contribution 2:	0.8 m/s @ 3.1415 rad
ω_n $\forall$ Reference Models:	1.6
ζ $\forall$ Reference Models:	1
T $\forall$ Numerical Derivatives:	2
Desired Depth (z_r):	10 m

Table 8.1: Simulation Parameters

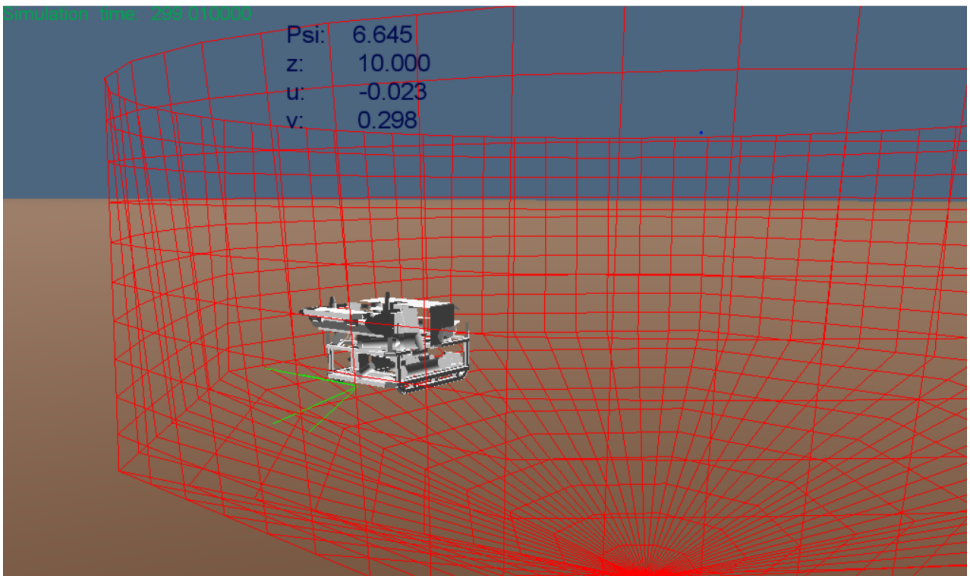

Figure 8.1: FhSim Simulation Environment

8.1.1 ARGUS Mini ROV Parameters

The ARGUS Mini ROV has previously been used in SINTEF research projects and NTNU masters theses [10][20]. Therefore, the parameters required to simulate the ARGUS Mini are already available. These parameter matrices were provided by SINTEF Ocean for use in this thesis.

$$
\begin{aligned}
\boldsymbol{M_{RB}} &= \text{diag}(90, 90, 90, 10, 15, 13) \\
\boldsymbol{M_A} &= \text{diag}(54, 72, 360, 11, 43.5, 5.2) \\
\boldsymbol{D} &= \text{diag}(250, 200, 175, 20, 20, 15) \\
\boldsymbol{D_{nl}} &= \text{diag}(350|u_r|, 350|v_r|, 400|w_r|, 100|p|, 100|q|, 75|r|) \\
\boldsymbol{g(\eta)} &\approx \begin{bmatrix} -0.91\sin(\theta) \\ 0.91\cos(\theta)\sin(\phi) \\ 0.91\cos(\theta)\cos(\phi) \\ 0.18\cos(\theta)\sin(\phi) \\ 0.18\sin(\theta) \\ 0 \end{bmatrix}
\end{aligned} \tag{8.1}
$$

8.2 Simulation Results

Both controllers developed were simulated using the FhSim simulation setup presented in Section 8.1. Any changes from this setup will be detailed wherever relevant. All gains and parameters used will be presented for the relevant controller. The controller gains used in the simulations are presented in Table 8.2.

In addition to plots showing the controller performance the root-mean-square error (RMSE) will be presented. RMSE is a way of showing the tracking error of the controller and can be used to better compare controller performances. This method was also used in the project report, [8], and can be read more about there. The equation giving the RMSE value is:

$$
RMSE = \sqrt{\frac{1}{n}\sum_{i=1}^{n}\tilde{x}^2} \tag{8.2}
$$

where $\tilde{x} = x_{i_{ref}} - x_{i_{measured}}$ [8, Chapter 2.3]. In order to make the RMSE values comparable all values will be calculated from using the same number of data points starting at a value where the system is attempting to track its reference. This is done to remove any potential bias caused by different amounts of data points or by selectively choosing data where one controller has settled while the others have not. This makes all the data presented easier to compare. Table 8.3 shows the RMSE values for all controller responses presented in this chapter. Note that the heading RMSE value will be calculated using radians, not degrees. Low RMSE values mean the controller is tracking the reference well.

GSTA Controller Gains

	k_1	k_2	β
Heading:	2	0.008	25
Surge:	0.5	5	25
Sway:	0.5	5	25
Depth:	25	0.001	30

(a) GSTA Controller Gains

Adaptive GSTA Controller Gains

	β	ω	γ	ε	λ	α_{tol}
Heading:	25	15	10	0.0001	0.001	0.05
Surge:	25	6	3	0.0001	5	0.03
Sway:	25	6	3	0.0001	5	0.03
Depth:	30	3	4	0.00001	0.001	0.05

(b) Adaptive GSTA Controller Gains

Table 8.2: Controller Gains: Simulation

RMSE

	GSTA	**AGSTA**
Distance:	0.6217 [m]	0.6206 [m]
Heading:	0.0077 [rad]	0.0028 [rad]
Surge:	$5.82 \cdot 10^{-4}$ [m/s]	$5.07 \cdot 10^{-4}$ [m/s]
Sway:	$5.55 \cdot 10^{-4}$ [m/s]	$4.62 \cdot 10^{-4}$ [m/s]
Total Velocity:	$5.85 \cdot 10^{-4}$ [m/s]	$5.08 \cdot 10^{-4}$ [m/s]
Depth:	0.0174 [m]	0.0124 [m]

(a) Without Numerical Derivatives

RMSE

	GSTA	**AGSTA**
Distance:	0.5978 [m]	0.5909 [m]
Heading:	0.0077 [rad]	0.0027 [rad]
Surge:	0.0015 [m/s]	0.0015 [m/s]
Sway:	$4.64 \cdot 10^{-4}$ [m/s]	$3.90 \cdot 10^{-4}$ [m/s]
Total Velocity:	$4.41 \cdot 10^{-4}$ [m/s]	$4.65 \cdot 10^{-4}$ [m/s]
Depth:	0.0215 [m]	0.0277 [m]

(b) With Numerical Derivatives

Table 8.3: Simulation: RMSE Controller Values

8.2.1 GSTA Controller Performance

This section presents the simulation results of the GSTA controllers. The controllers are first tested without the use of the numerical estimation of the unmeasured states. This test shows how the controller performs when all required states are properly measured using a sensor. The feedback data in this test will therefore be taken directly from the process plant. In the second test the controllers will use the numerical differentiation method to estimate the lacking sensor data. This test shows how the controllers perform when the ROV is equipped with limited sensors, as it would be under real-world operations. Additionally, the second test verifies the functionality of the numerical estimation method. The output data from the numerical differentiation is not presented in this

chapter, these results are presented and discussed in chapter 10.4.

Without Numerical Derivatives

Figures 8.2-8.4 shows the performances of the controllers tracking the static net-pen using the standard simulation parameters. These plots show the performance of all the controlled states.

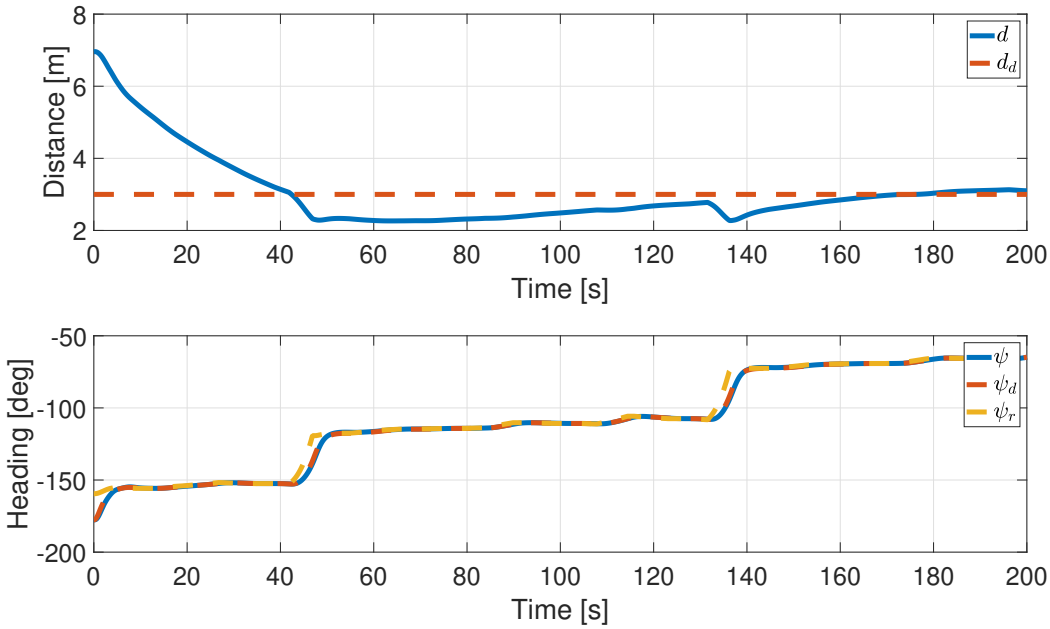

Figure 8.2: GSTA w/o Estimates: Distance and Heading Plots

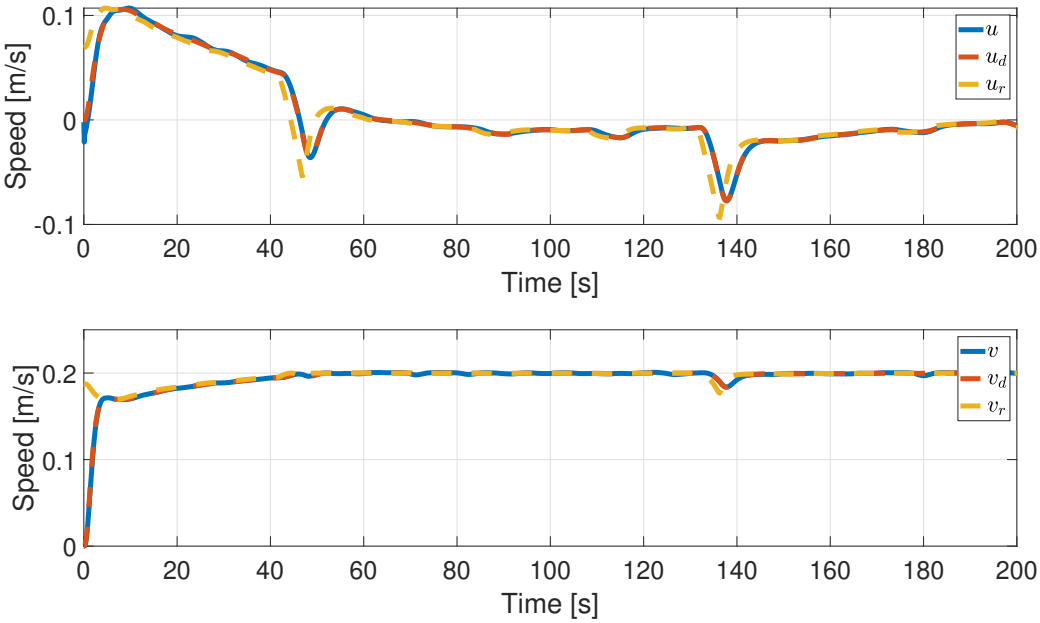

Figure 8.3: GSTA w/o Estimates: Surge and Sway Plots

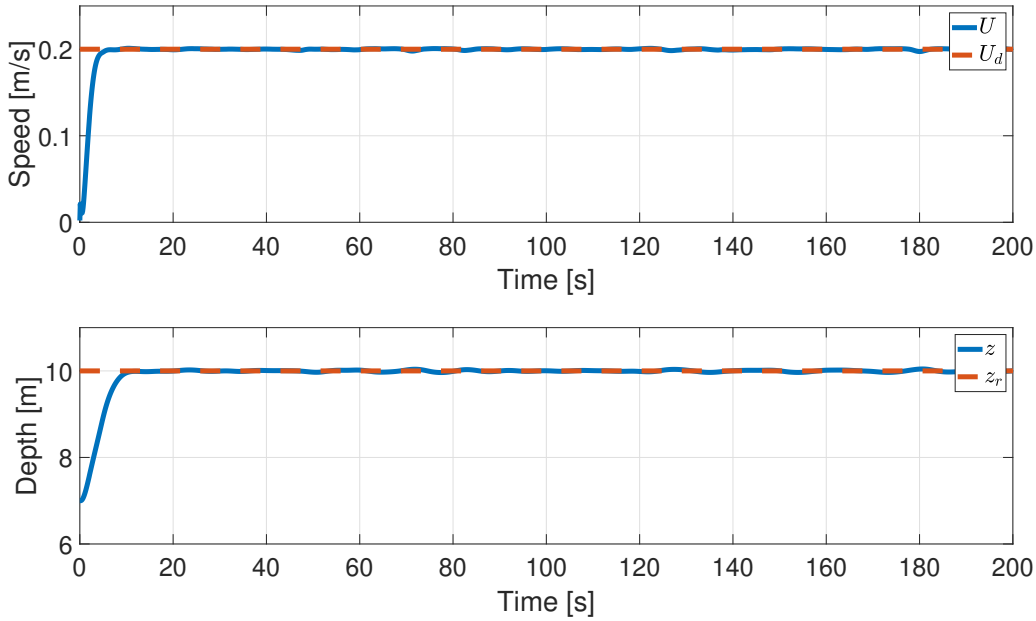

Figure 8.4: GSTA w/o Estimates: Total Velocity and Depth Plots

With Numerical Derivatives

Figures 8.5-8.7 show the results from the GSTA controllers when simulating using the parameters given in Table 8.1, while using the filtered numerical derivatives to estimate the unmeasured states.

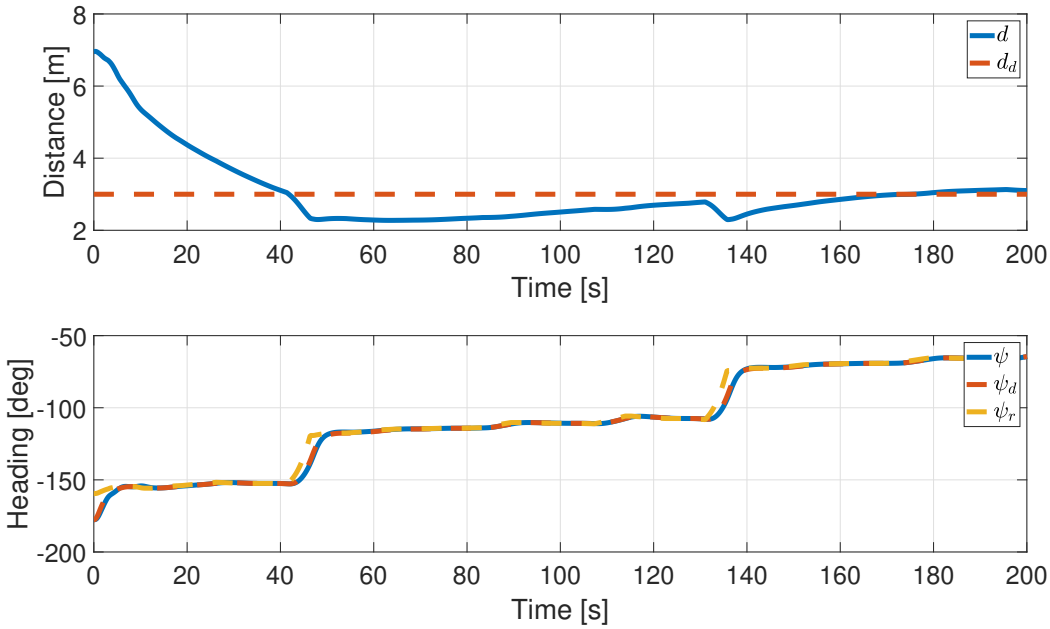

Figure 8.5: GSTA: Distance and Heading Plots

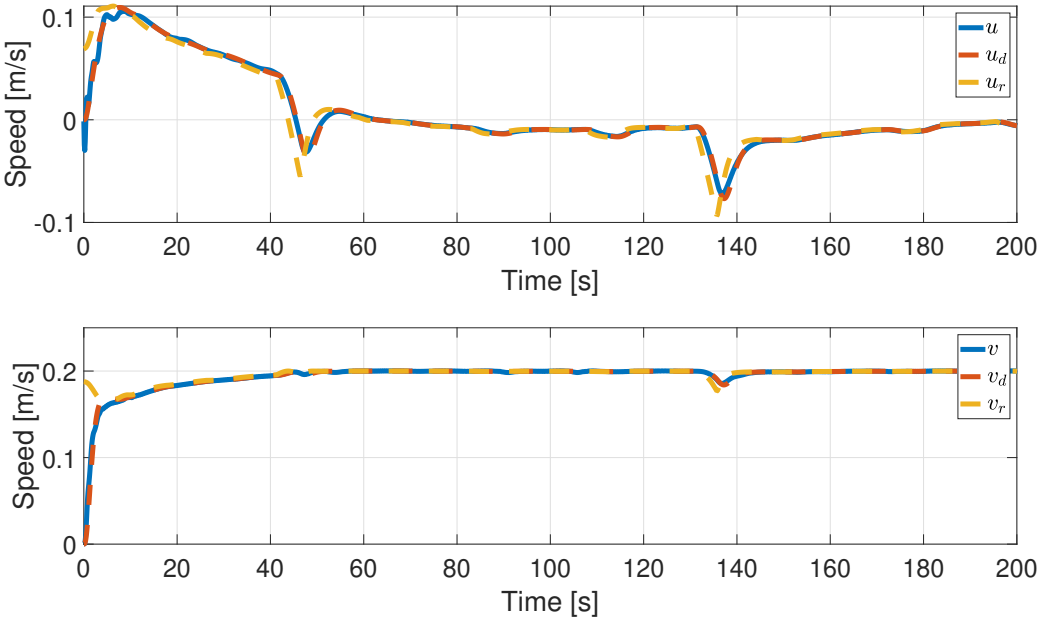

Figure 8.6: GSTA: Surge and Sway Plots

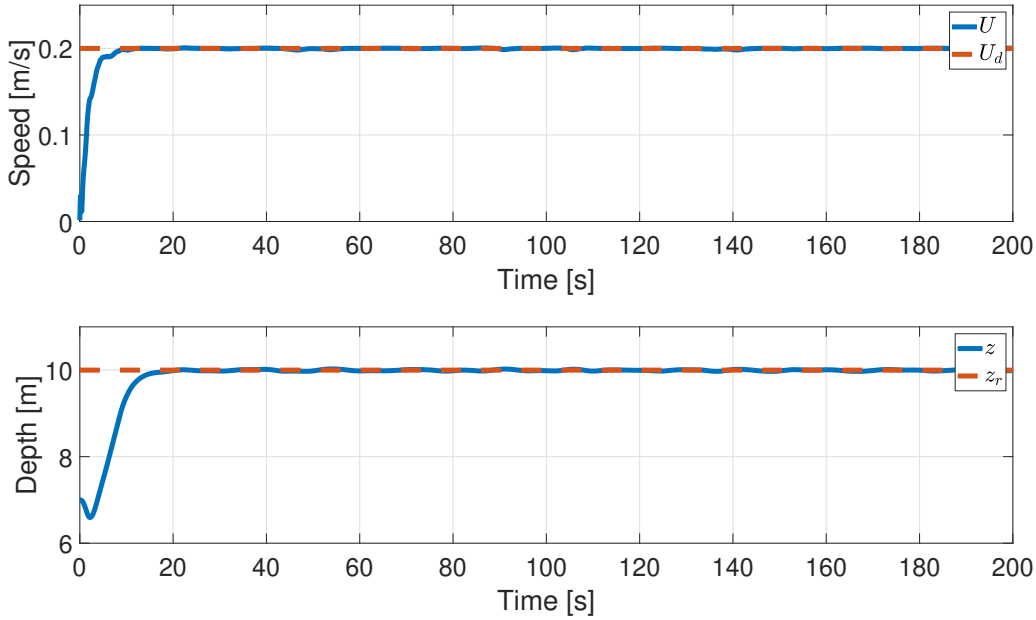

Figure 8.7: GSTA: Total Velocity and Depth Plots

8.2.2 Adaptive GSTA Controller Performance

Similarly to the GSTA simulations, the adaptive GSTA is first simulated using direct feedback from the process plant in all required states, then the numerical estimates are

used in the second test. This is done to first show the controllers behaviour with all required measurements available, then to show the behaviours with the estimator required for the ROV used in this project.

Without Numerical Derivatives

Figures 8.8-8.10 presents the adaptive GSTA controllers' performances during a simulation using the same parameters and setup as the GSTA test.

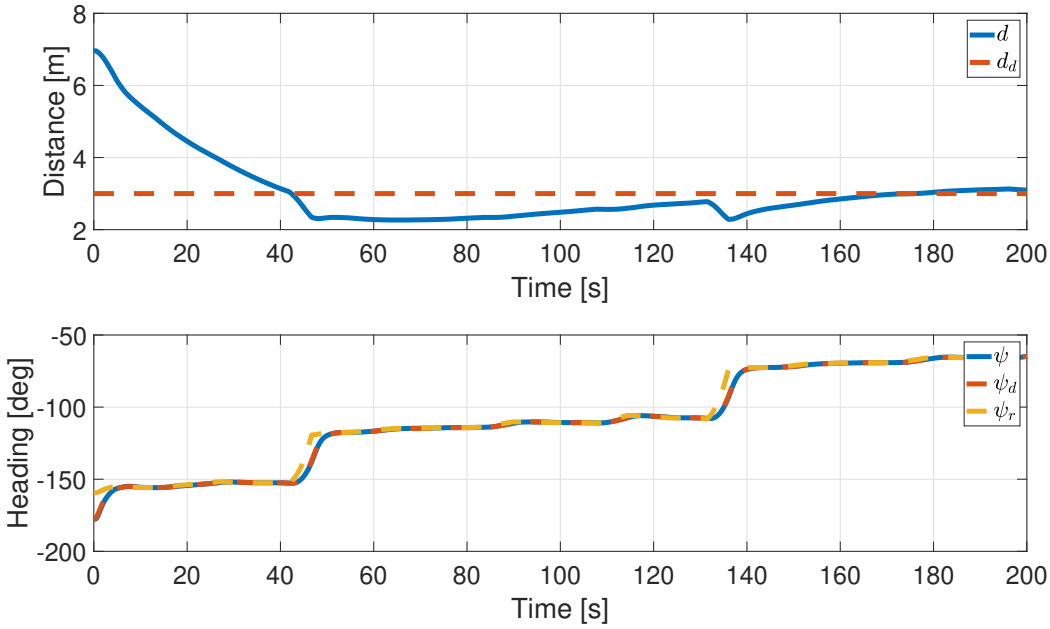

Figure 8.8: Adaptive GSTA w/o Estimates: Distance and Heading Plots

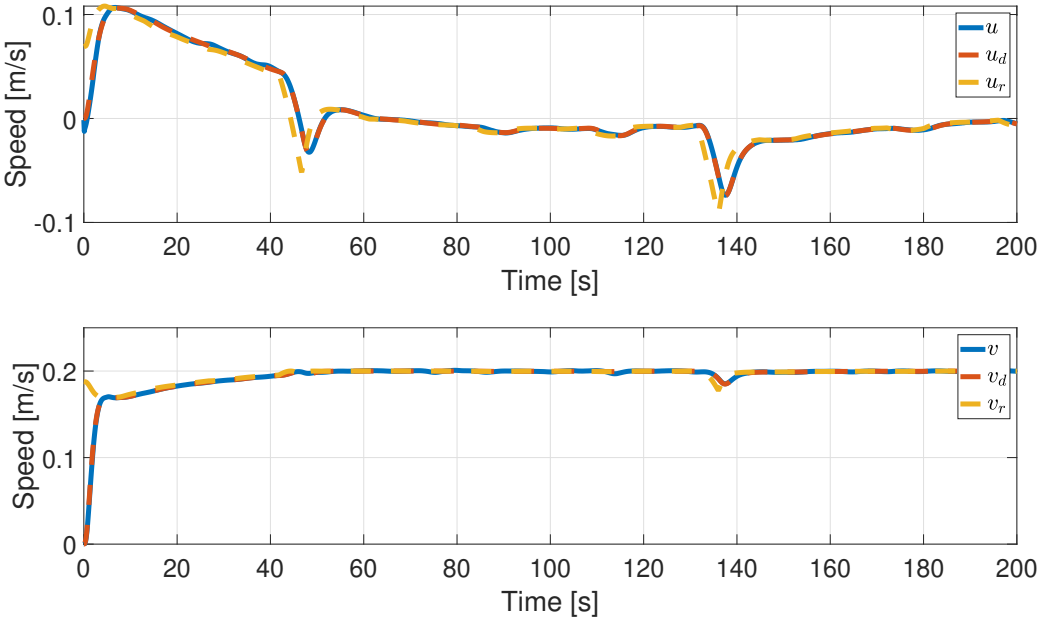

Figure 8.9: Adaptive GSTA w/o Estimates: Surge and Sway Plots

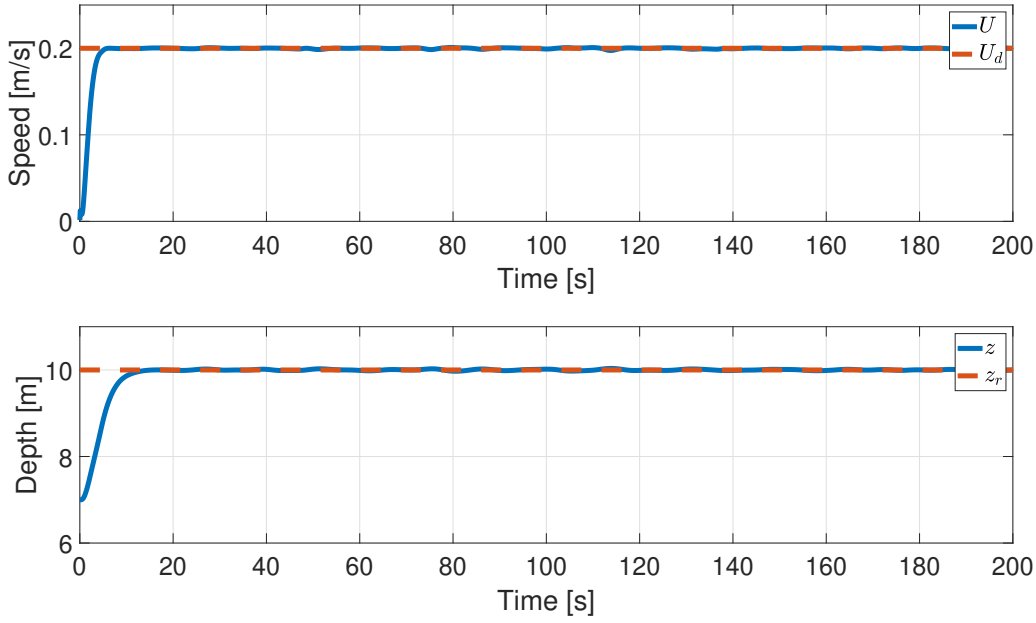

Figure 8.10: Adaptive GSTA w/o Estimates: Total Velocity and Depth Plots

With Numerical Derivatives

Figures 8.11-8.13 presents the adaptive GSTA controllers' performances while using the numerical estimates as feedback for the unmeasured data.

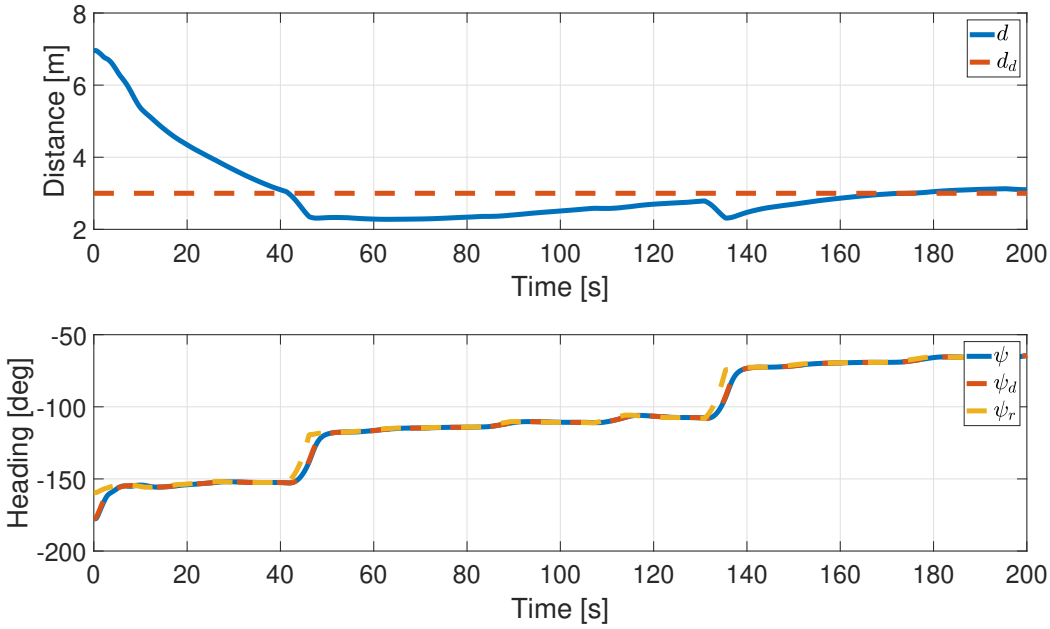

Figure 8.11: Adaptive GSTA: Distance and Heading Plots

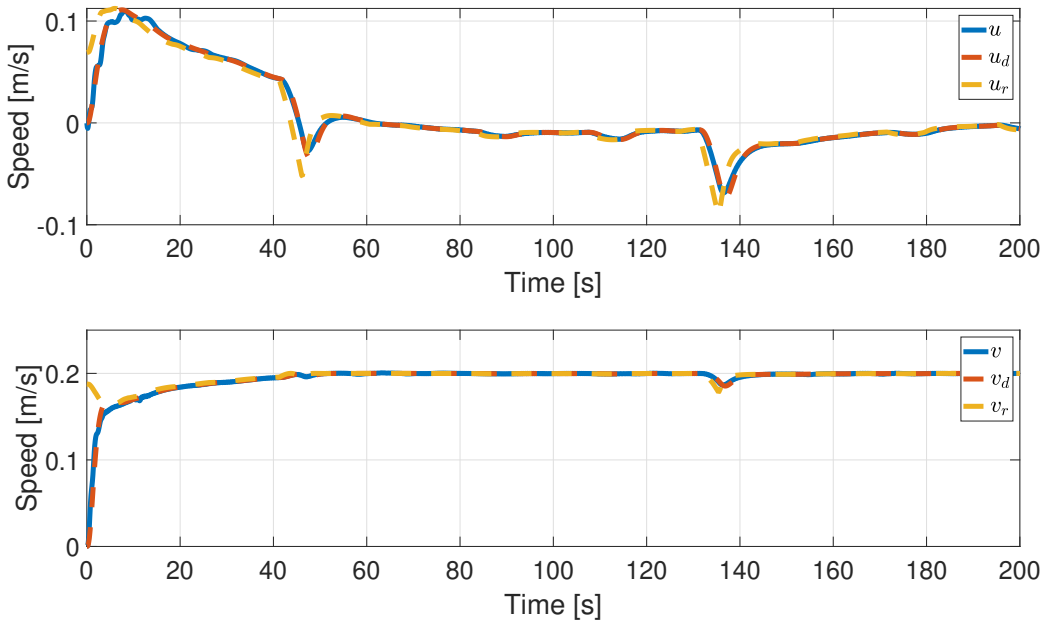

Figure 8.12: Adaptive GSTA: Surge and Sway Plots

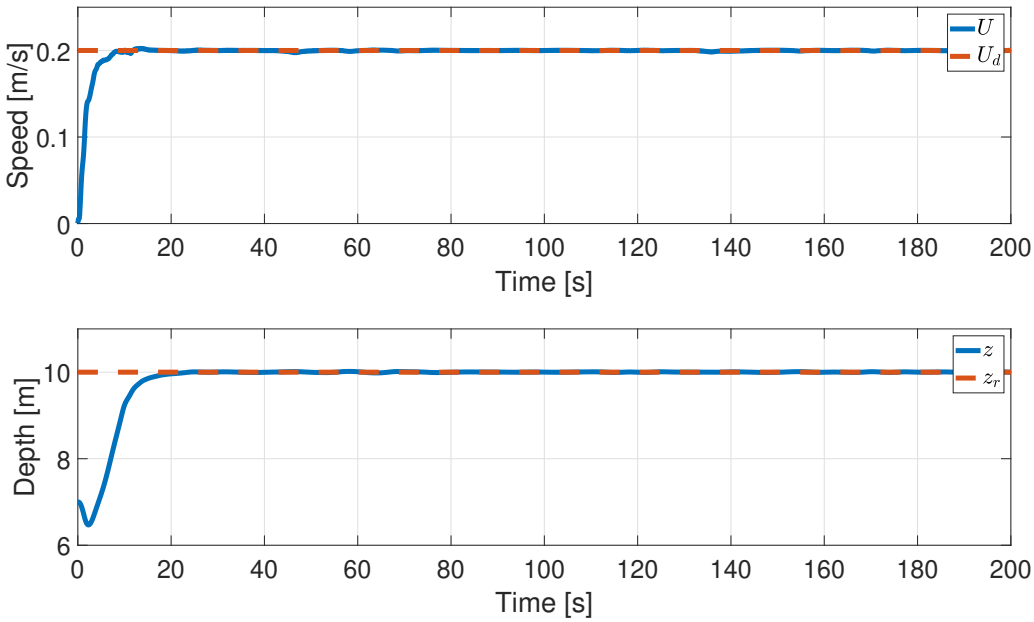

Figure 8.13: Adaptive GSTA: Total Velocity and Depth Plots

Chapter 9

Field Test Results

9.1 Test Setup

To validate the controllers' performances, full-scale field tests were performed. Similarly to the simulation results, these tests used the ILOS algorithm and DVL to follow an aquaculture net pen at a certain distance. The tests were performed using the ARGUS MINI ROV equipped with a DVL. This ROV is the physical version of the ROV model described in Section 8.1. The test was done at the SINTEF ACE full-scale aquaculture laboratory, which has an exposed aquaculture fish farm. This makes it possible to test the controllers' ability to autonomously traverse an aquaculture net pen with fish in it. Additionally, it is able to test the controllers' performances in an area exposed to time-varying ocean and wave disturbances. This means the field test is a proper validation of the controllers' performances in the exact environment they were designed for.

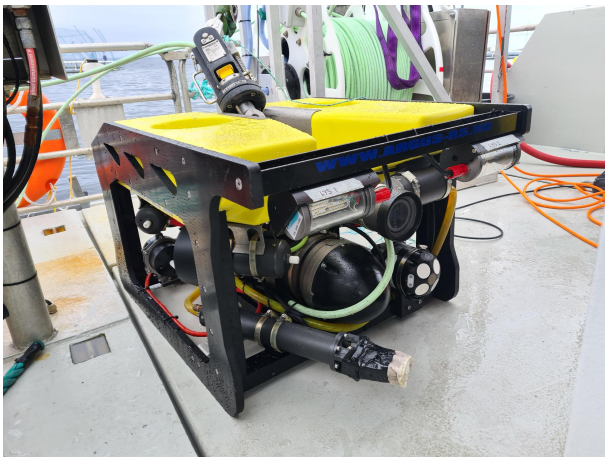

Figure 9.1: Argus Mini ROV with DVL. Image courtesy of Bent Oddvar A. Haugaløkken.

Table 9.1 presents a few notable parameters used for the field test. The environmental conditions acting within the net pen during the test were not documented with empirical values. The wind in the area was a gentle breeze during testing. The ocean current in the net pen was described by the ROV test operator as "quite strong", the ROV camera view

was described as "limited", and the overall test conditions were described as "tough". The main factor making the test conditions tough were the fish within the pen. The ocean current outside of the net pen had a mean value of approximately 0.1 [m/s] at a depth of 5 [m], but this is not necessarily representative of the conditions within the net pen as the fish can make this disturbance larger. The fish were also obstructing the view of the DVL quite a bit, making the velocity reference oscillatory. At some points the DVL measurements were lost due to the fish obstructing the view. The results presented are the best tests from each controllers in the conditions described. For the field tests second-order reference models with $\zeta = 1$ and $\omega_n = 5$ were used for the velocity references. The position and angle references used third-order reference models, with $\zeta = 2$ and $\omega_n = 3$ for the heading reference and $\zeta = 1$ and $\omega_n = 3$ for the depth reference.

Test Parameters:	
Net Follow Distance (d_d):	3 m
Desired Total Velocity (U_d):	0.2 m/s
Wind Speed:	5 m/s
T $\forall$ Numerical Derivatives:	1

Table 9.1: Test Parameters

Figure 9.2: The SINTEF ACE full-scale Aquaculture Laboratory

9.2 Controller Results

For the field test a new set of controller gains were used. These were found through iterative testing of the controllers while in the field. The gains from the simulation were used as a starting point, but as the simulation environment is a model of the real world

differences will occur. The controller gains used for the following tests are presented in Table 9.2. For these tests the numerical estimation of the unmeasured states are used for the GSTA controllers.

GSTA Controller Gains

	k_1	k_2	β
Heading:	2	0.008	25
Surge:	0.5	5	5
Sway:	1	1	10
Depth:	25	0.001	15

(a) GSTA Controller Gains

PID Controller Gains

	k_p	k_d	k_i
Heading:	15	1	0.5
Surge:	200	0	5
Sway:	200	0	5
Depth:	100	0	1

(b) PID Controller Gains

Adaptive GSTA Controller Gains

	β	ω	γ	ε	λ	α_{tol}
Heading:	1	1	1	0.001	1	0.2
Surge:	6	1	5	0.0001	2	0.2
Sway:	6	1	5	0.0001	2	0.2
Depth:	5	1	3	0.00001	0.01	0.15

(c) Adaptive GSTA Controller Gains

Table 9.2: Controller Gains: Field Test

The RMSE values for all the results shown in this chapter is shown in Table 9.3. These values were found using the same method as in Chapter 8.2 where the same number of samples were taken for all calculations and the samples are taken from when the controller starts tracking the reference.

Field Trial RMSE Values

	GSTA	Adaptive GSTA	PID
Distance:	0.4023	0.6811	0.8204
Heading:	0.0900	0.0966	0.1446
Surge:	0.0539	0.0354	0.0483
Sway:	0.0774	0.0456	0.1032
Total Velocity:	0.0780	0.0546	0.1137
Depth:	0.1431	0.1131	0.0783

Table 9.3: Field Trial: RMSE Controller Values

9.2.1 GSTA Controller Performance

Figures 9.3-9.5 show the GSTA controllers' performances during the field test. The plots can be separated into three sections. First the desired total speed reference (U_d) is held at zero while the ROV reaches its desired depth, $z_r = 5.1$ [m]. Then the ROV starts following the net pen with $U_d = 0.2$ [m/s] and $d_d = 3.0$ [m] in a clockwise direction. About halfway through the test, the direction is changed and the ROV starts following the net in a counter clockwise direction.

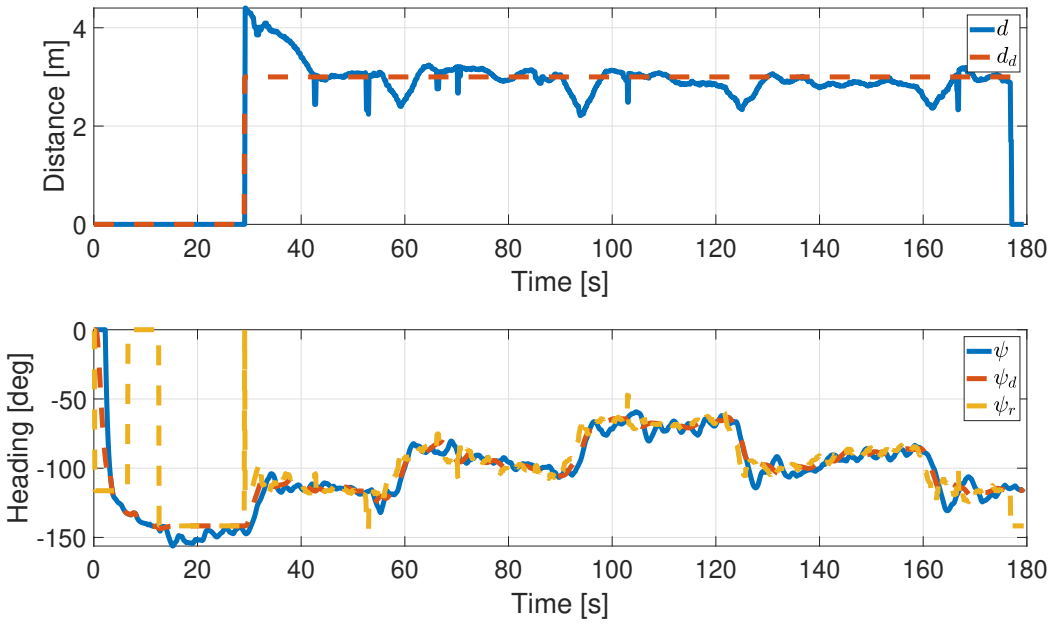

Figure 9.3: GSTA: Distance and Heading Plots

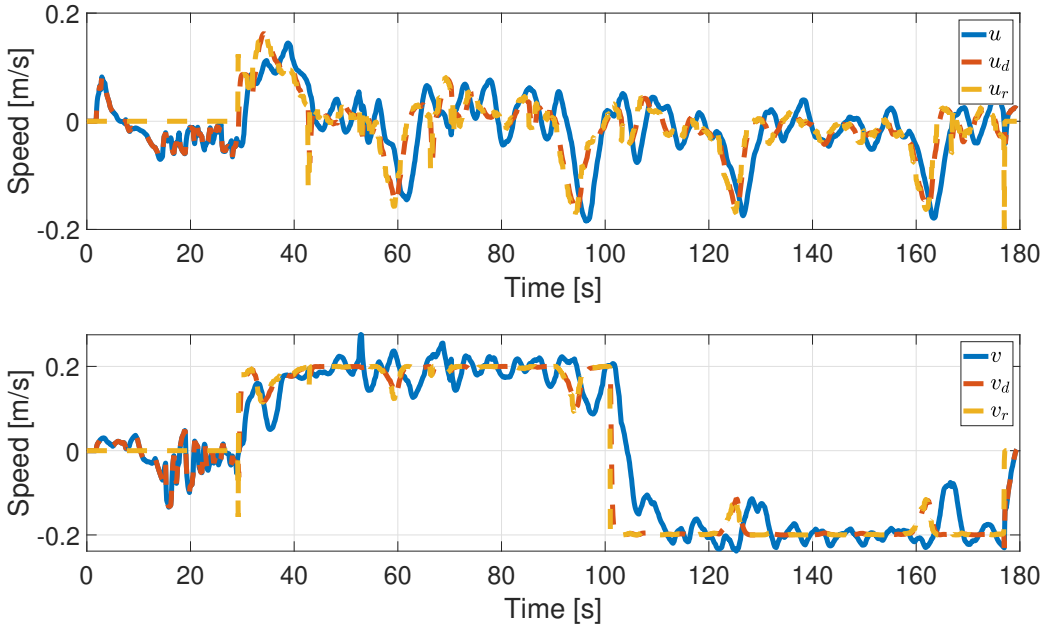

Figure 9.4: GSTA: Surge and Sway Velocity Plots

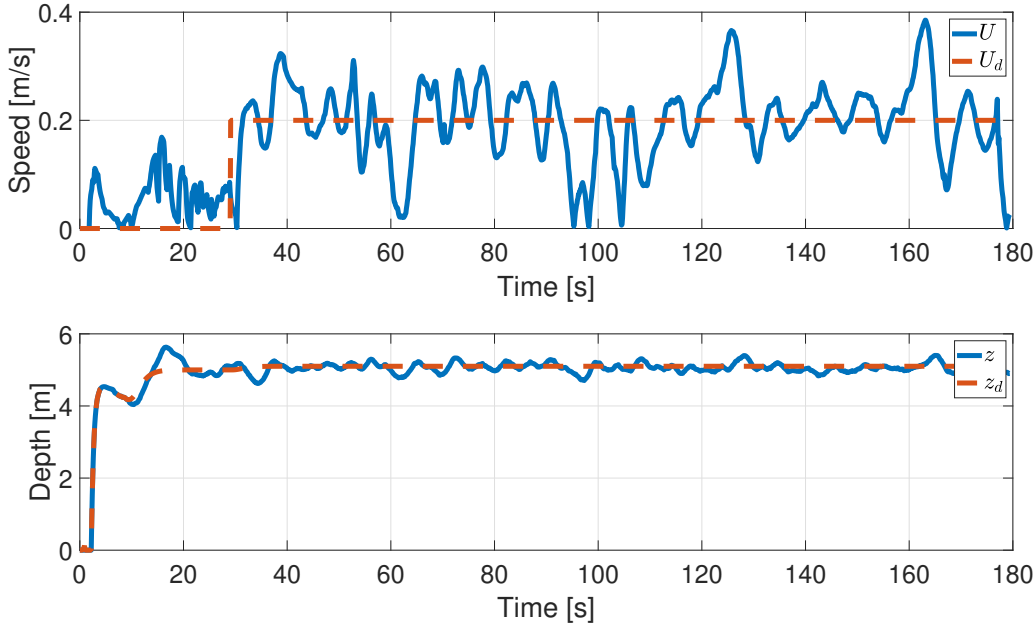

Figure 9.5: GSTA: Total Velocity and Depth Plots

9.2.2 Adaptive GSTA Controller Performance

Figures 9.6-9.8 show the adaptive GSTA controllers' performances during the field test. For test the depth reference was $z_r = 4.65$ [m]. Again, the ROV reached the desired

depth before the net-following was activated. Something to note about Figure 9.6 is that the sudden drops in d_d is caused by the DVL measurements being obstructed. When the system loses the DVL measurements the value drops to zero. This is the cause of the large and sudden jumps in the measured distance. Similar to the GSTA controller test, the desired total velocity is $U_d = 0.2$ [m/s], the desired following distance $d_d = 3$ [m], and the ROV changes direction around halfway through the test.

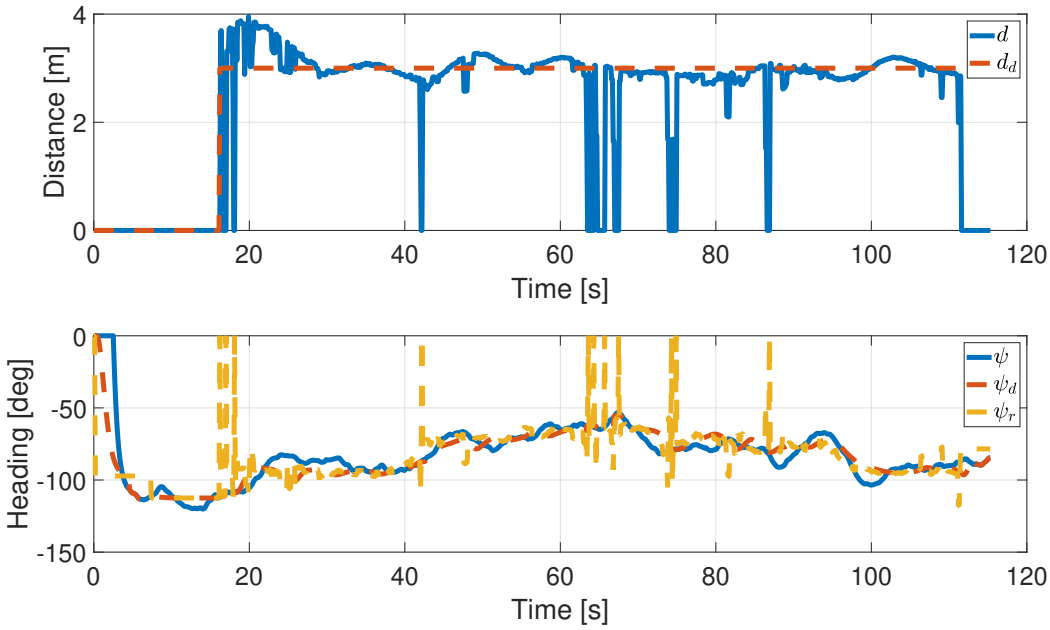

Figure 9.6: Adaptive GSTA: Distance and Heading Plots

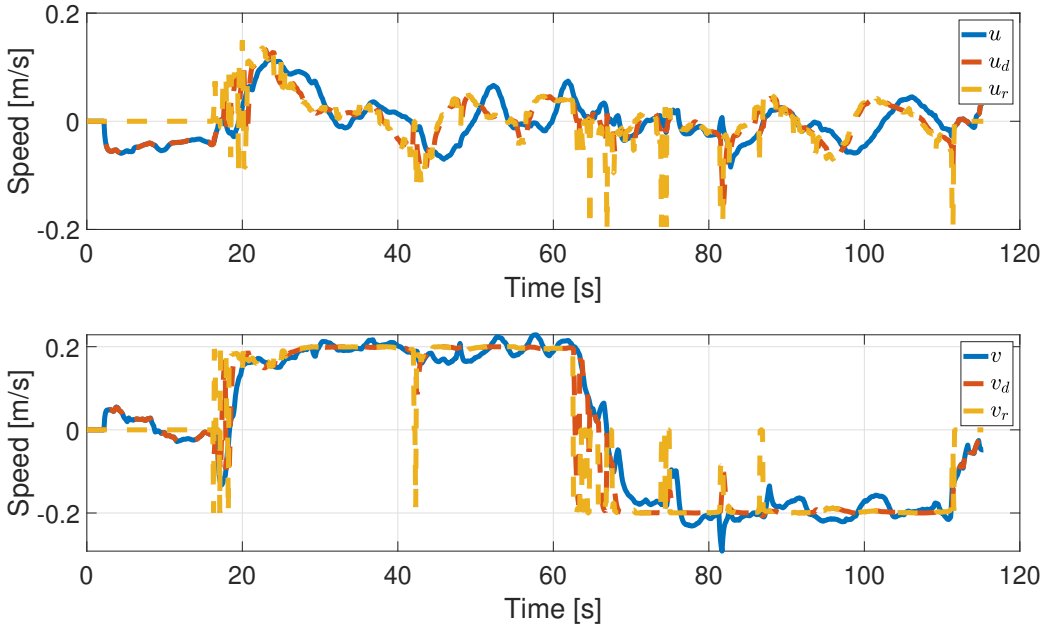

Figure 9.7: Adaptive GSTA: Surge and Sway Velocity Plots

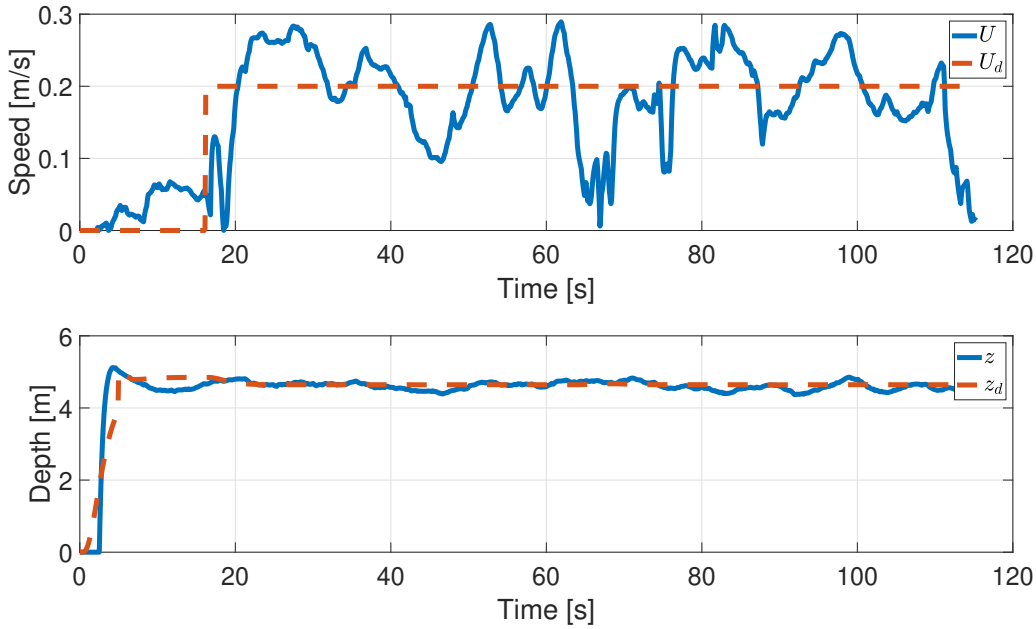

Figure 9.8: Adaptive GSTA: Total Velocity and Depth Plots

9.2.3 PID Controller Performance

Figures 9.9-9.11 show generic PID controllers' performances during the field test. Just like the GSTA based controllers the PID controllers are separate controllers for heading,

surge, sway, and depth allowing for 3D maneuvering of the ROV. This data is included to compare the GSTA based controllers performances to another control method. For this test $z_r = 3.65$ [m], the desired total velocity is $U_d = 0.2$ [m/s], and the desired following distance $d_d = 3$ [m]. Again, the sudden jumps in d_d (Figure 9.9) are caused by invalid DVL measurements.

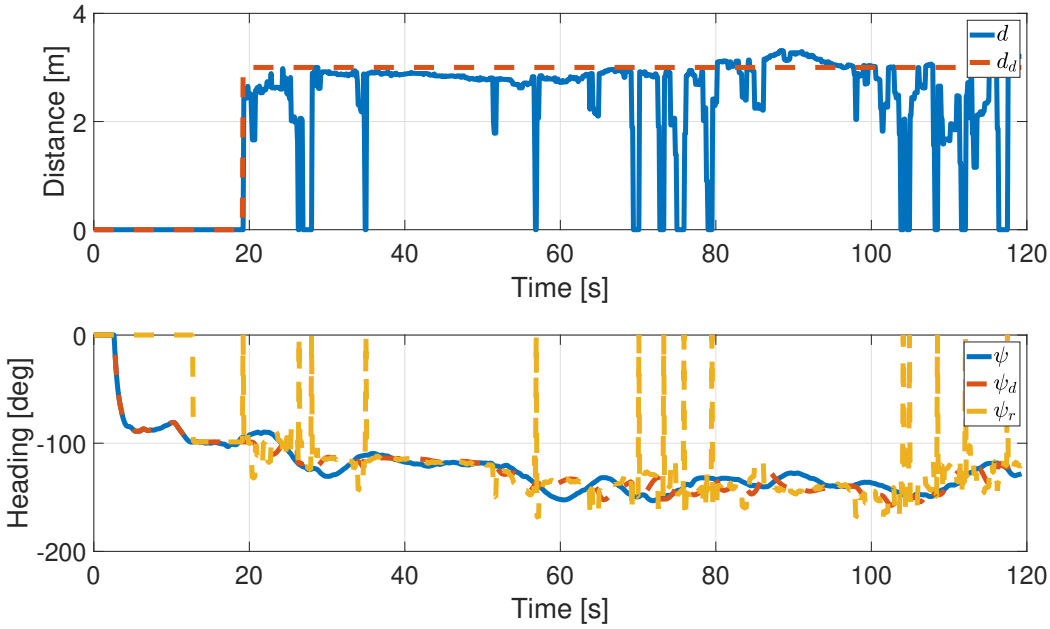

Figure 9.9: PID: Distance and Heading Plots

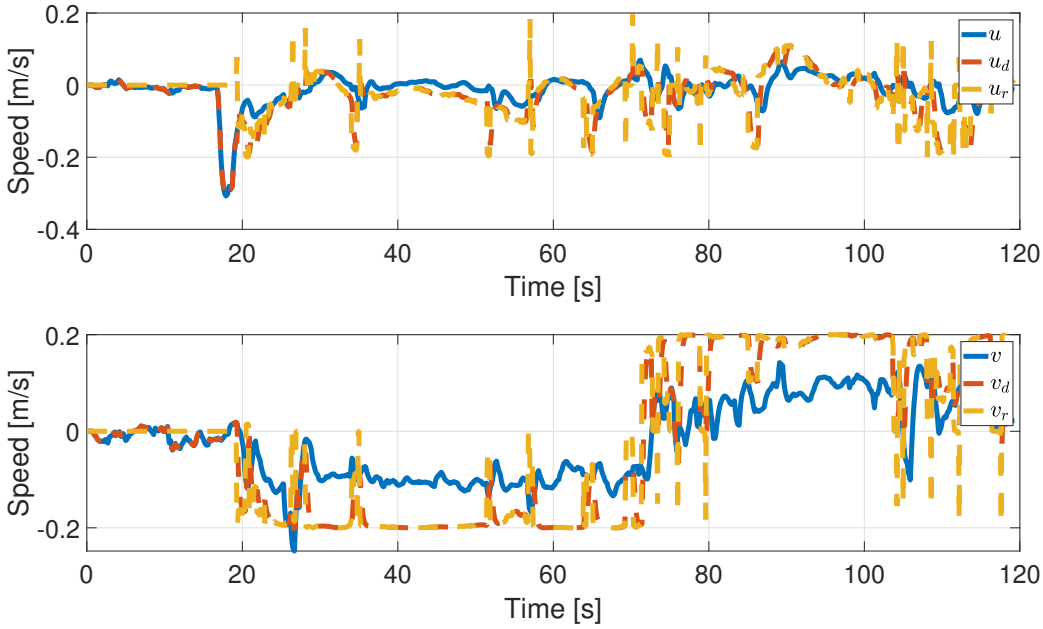

Figure 9.10: PID: Surge and Sway Velocity Plots

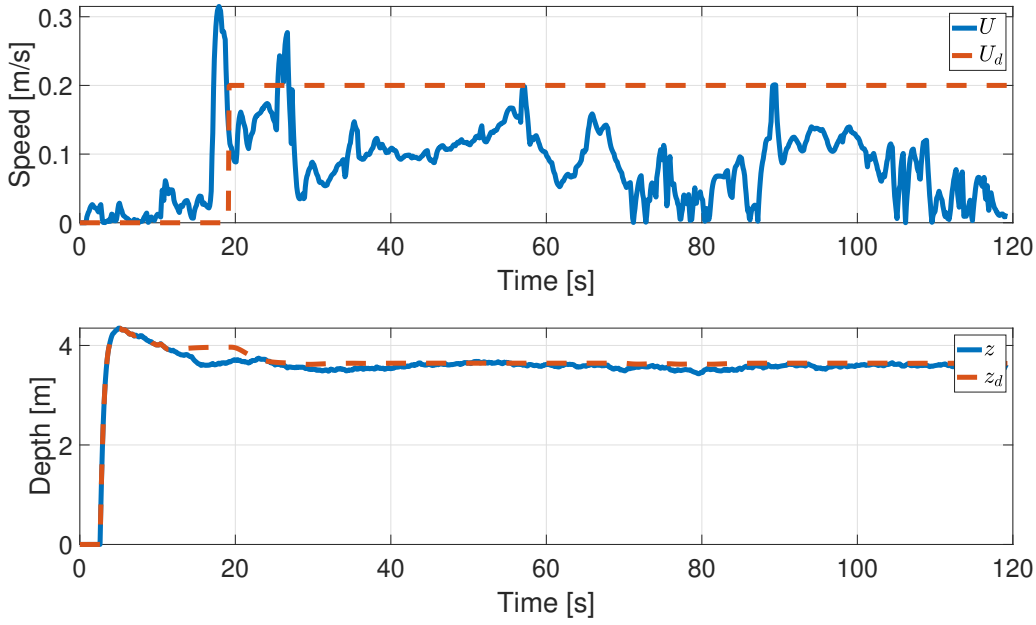

Figure 9.11: PID: Total Velocity and Depth Plots

Chapter 10

Discussion

10.1 Controller Performances

This sub-chapter discusses the controller results presented in the previous chapters. The goal is to discuss the controllers' performances, compare them to each other, and discuss the test setup and methods used to obtain the results. Like the result chapters, this discussion is split into two main parts to divide simulation results and results from the field test.

To obtain comparable RMSE values the RMSE analysis for each controller used the same number of data points in an area where the controller was tracking the reference. This means the RMSE numbers do not give any information about the system's initial transient behavior. This was done purposely, as the transient behavior of a controller is easier to analyze visually using plots, while the tracking performances of the different controllers can be hard to compare visually. Fair selection of result data was especially important for the field test results, considering that the physical tests vary slightly in how they start and end. The field tests could have manual operator control or intervention before and after the net pen tracking starts, meaning these parts of the tests are not necessarily directly comparable. The RMSE values will be used in this discussion as a measure of how well the system is able to track its slow-moving reference and will be directly compared to other controllers of the same type. This method of comparison is considered justifiable due to the way the values were calculated.

10.1.1 Simulation

The simulation environment worked as intended and was able to properly simulate a net pen tracking operation for an ROV. This made it possible properly validate the controllers' performances before exposing them to a field test. This way of verifying controllers is a great way of making sure potential real-world operations go without issues and proved to be a valuable asset during this project.

The environmental simulation conditions presented in Chapter 8.1 were chosen to mimic normal conditions at an exposed aquaculture site in Norway. Keep in mind that

these conditions are meant to give a baseline for the controllers' normal performance. No limit testing robustness analysis has been done concerning the controllers' abilities to manage rough environmental disturbances, as these are not normal operating conditions for this ROV. This type of analysis is left as further work. Appendix C shows an example of the controllers' performances with higher environmental disturbances, these figures are meant as a visual example showing performance in rough conditions. In this example the significant wave height is 2.5 [m], the mean wave period is 5 [s], and the total current is 1 [m/s]. According to [2], these are conditions experienced at the most exposed aquaculture sites in Norway, alongside a low mean wave period. The results seen in Appendix C are promising, indicating that after a proper robustness analysis and limit test, the controllers developed in this thesis can help expand the operational weather window for operations at exposed aquaculture sites.

The purpose of the simulations was to validate the controllers' stability and performance before doing a field trial. These simulations were highly successfully giving promising results for both the fixed gain GSTA and adaption gain GSTA variations of the controllers. It can be seen from the plots in Chapter 8.2 that the controllers track the reference model's output very well. Additionally, the RMSE values show little to no error for all the controllers. These results are very promising for the performance of the controllers. Something to note is that the adaptive GSTA controllers are slightly better at tracking the reference, which can be seen in the RMSE values in Table 8.3. It is important to note that this is the response after the adaptive gains have converged to their desired values, meaning any potential poor behavior during the first few seconds of operation is not considered. By comparing the behavior of both controller types during the first few seconds it seems like the adaptive controllers give little to no disadvantage over the fixed-gain controllers. This is a great result for the adaptive gains, as a poor initial response could potentially be a problem if the adaptive gains are poorly tuned. The gains used in simulations immediately gave decent controller performance during the field test, meaning the simulation model worked well as a test environment to tune and verify the controller performances.

Looking at the results using the numerical estimates it is clear that the initial performance for both versions of the controllers is worsened. Small oscillations in the states can be seen in the plots, which is a direct cause of the numerical estimates not having converged. This behavior disappears quickly and is further discussed in Chapter 10.4. The distance plots have the highest RMSE values for both controllers. This is caused by the guidance system, not the controllers. Though this is the largest error, the total tracking of the net pen is excellent and the ROV is able to complete net-following operations with high accuracy. All in all, the simulation results for both controller types were excellent, verifying the controllers' stability and performance, and providing a good starting point for field trials.

10.1.2 Field Test

Though wind and wave conditions outside of the net pen during the field tests were relatively calm, the test conditions were still quite tough due to a high fish activity within the net pen. The fish obstructed the DVL quite a bit during the net-following, making the velocity references quite oscillatory. In some cases, the DVL was not able to produce a net plane approximation due to having less than three reference beams. The high fish activity also creates additional ocean currents within the net and limits the operator's view. These effects combined created a tough testing environment. Unfortunately, no measurements were made of wave height or ocean current within the net pen during the tests, making it hard to describe the conditions accurately. Even though the test conditions were tough they depicted how test conditions are in real life, ultimately creating a good test environment to see how the controllers perform in the real world.

The GSTA based controllers performed very well in the field trial. Looking at the plots and the RMSE values it is clear that while the performance was worse than the simulations, both controller types were able to follow their references. This meant that the overall net-tracking of the ROV was successful, which can be seen by looking at the distance and heading plots (Figure 9.3, Figure 9.6). Both the fixed-gain and adaptive GSTA surge and sway controllers struggle a bit more. The surge reference value is rapidly changing, and the controller response is slightly oscillatory trying to follow the oscillating reference. The sway reference is calm compared to the surge reference, but the controller response is sway is also slightly oscillatory. Looking at the surge and sway RMSE values for the adaptive and fixed gain GSTA controllers it is clear that the tracking is not perfect. This means that while the ROV is able to follow at the desired distance from the net pen, it is not able to perfectly track the total desired velocity. This is also seen in the total velocity plots for the controllers, as it oscillates around the reference. Note that the biggest dip in total velocity for all total velocity plots is when the reference changes, this is to be expected as the ROV has to slow down and accelerate in the opposite direction upon the reference change. A trend for all controllers is that the sway velocity controller has a slightly higher tracking error when compared to the surge controller. This is likely due to the surge reference being approximately zero while tracking the net while the sway velocity reference is less static. All in all, both GSTA based controllers were able to accurately follow the net pen as desired, but due to various environmental effects and DVL obstructions the total velocities were oscillatory.

One issue with the adaptive heading controller during the field test was the tuning of the adaption law. Looking at Figure 10.1 it is possible to see that at some points the controller leaves $\sigma_\psi = 0$ and the gains are updated. This is the controller trying to keep the system in sliding mode. This is not ideal, as it likely means that the controller gains are too low to accurately follow the reference. This is likely the cause of the poor tracking and high RMSE value for heading in the adaptive GSTA field test results, compared to the GSTA results. This issue can be fixed by increasing the total value of $\omega\sqrt{\gamma/2}$, as this will make the controller gains increase quicker. Note that there is an upper limit to this as if the adaption law chooses too high gains instability may occur. This issue, regarding

too low adaptive gains, is further discussed in Chapter 10.2. Even with the poor tuning, the adaptive GSTA heading controller outperformed the PID controller.

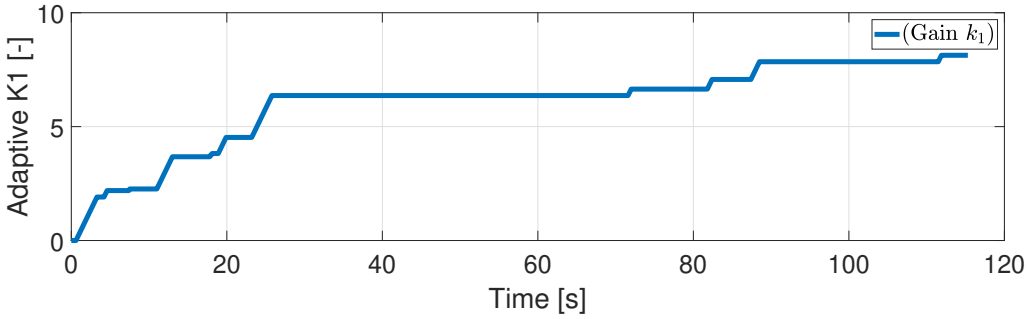

Figure 10.1: Field Test: Adaptive Heading Gain K1

Comparing the velocity controllers' performances of both the GSTA and adaptive GSTA to the PID velocity controller it is clear that the GSTA based controllers outperform the PID controller. The PID controller struggles to reach its desired total velocity (Figure 9.11) due to a very poor tracking in sway (Figure 9.10). The PID does however have a lower RMSE value for the surge controller when compared to the fixed gain GSTA controller. The PID depth controller is the only PID based control law consistently outperforming the GSTA based controllers. Here the PID depth controller is able to track the reference very well, while both GSTA based controllers are less accurate. This is the only regulated DOF where the PID controller is noticeably better than the GSTA controllers.

To summarize, the GSTA based controllers performed very well during the field test. They were able to follow the net pen accurately. The main issue with the controllers was the oscillations in the velocity controllers, caused by several factors. Even with the oscillating total velocity, the GSTA controllers were able to accurately track the net pen. The PID controllers showed the same issues with oscillations, only they were not able to reach the desired total velocity, making this control strategy less accurate in comparison. The only PID controller outperforming both GSTA controller types was the depth controller. Overall, the GSTA controllers showed a reliable performance and were able to operate with acceptable accuracy in the conditions they were designed for.

10.2 Tuning the Adaptive Gains

The purpose of the adaptive gain GSTA controller is to be able to keep the system in sliding mode by using adaptive gains. This works well when the adaptive gains are properly tuned. When implementing this controller, the hope was that tuning would require little effort, as the adaption law would be able to handle itself. This was not always the case. One observation made was that if the controller was tuned with too low gains some controllers would constantly fall out of sliding mode. This was especially noticeable in

the heading controller, as it experiences periodic noticeable changes in reference. When the heading controller had too low adaptive gains it would be unable to accurately follow the reference model, falling out of sliding mode on every change in reference. Once this happened the adaption law increased the gains, but not enough to solve the issue. This trend would go on for thousands of seconds until the controller found proper gains and was able to keep the system in sliding mode. The solution to this was tuning the adaption law more aggressively, allowing it to find better-suited gains from the get-go. This means that the implementation of the adaptive controller turned out to be similar to the fixed gain variant, where controller-specific tuning was required to obtain an acceptable performance from the controllers. The benefit of the adaptive gains is then the fact that it can update the gains, keeping the controller in sliding mode, not the simplicity of tuning.

Another issue with the adaption law is that the gains are unintuitive to tune. This can make the tuning process hard on the designer. This issue can be made better by choosing ε and ω carefully. Choosing a low value of ε will make it so k_2 is predominately chosen through λ. This makes k_2 less dependent on k_1 and allows the designer to focus on tuning the gains for $\dot{k}_1$. $\dot{k}_1$ decides how quickly the adaption law updates k_1. This rate should be chosen carefully, as tuning too aggressively can cause actuator strain and in some cases stability issues. On the other hand, not having large enough gains creates a problem where the gains never reach an acceptable value. A good balance must be found, which is best done through simulations. If desired, $\omega\sqrt{\gamma/2}$ can be changed to some constant ω creating fewer variables. This changes the adaption law to:

$$\dot{k}_1 = \begin{cases} 0 & if|\sigma| < \alpha_{tol} \\ \omega & otherwise \end{cases}, \tag{10.1}$$

$$k_2 = 2\varepsilon k_1 + \lambda + 4\varepsilon^2. \tag{10.2}$$

10.3 Choice of Sliding Variable

The depth controller has a different sliding variable than the other controllers due to stability benefits with lower gain values. These benefits were seen in the early project simulations. Using low gain values on the depth controller often resulted in the system oscillating around the desired reference value when in sliding mode. This behavior is not ideal, as a poorly tuned adaptive controller could have trouble converging to the depth reference, or in the worst case never reach it. This behavior was found in the early simulations of the project. It was therefore decided to use Equation (7.1b) as the sliding variable for depth. This sliding variable was inspired by the suggested sliding variable for $n = 3$ presented in Equation (4.4). This change removed the oscillations seen with low gains and made both GSTA based depth controllers more robust to poor tuning.

10.4 Numerical Derivatives

A numerical derivative method was implemented to estimate the missing sensor data. This method, using a high-pass filter, worked well. Comparing the simulation results with and without the numerical derivatives show that the results are practically identical. Figure 10.2 is an example of the numerical estimates plotted against the actual plant values for the velocities in surge and sway. The method has some troubles initially but is quickly able to accurately estimate the desired states. The effects of the initial poor estimates can be seen by comparing Figure 8.3 and Figure 8.6, as both surge and sway experience minor oscillations when the estimate is oscillating. This effect disappears quickly, and after a few seconds, the system with the numerical derivatives tracks the reference perfectly.

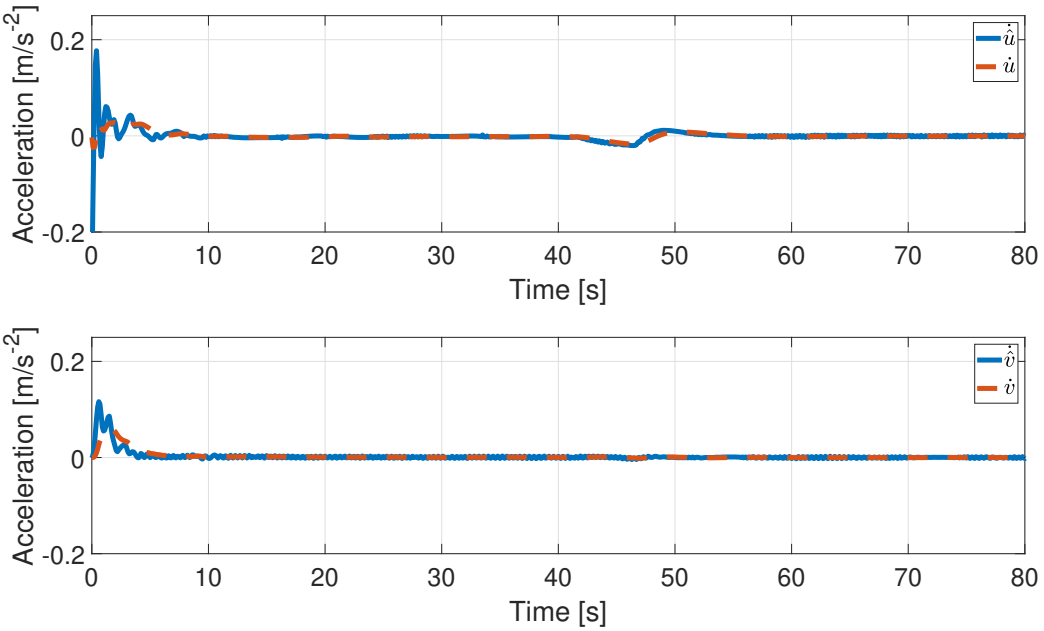

Figure 10.2: Simulation: Numerical Estimates

One issue with using a high-pass filter to take numerical derivatives is that it introduces a phase shift to the signal. This phase shift is dependent on the time constant of the high-pass filter. This is not an issue, but if the total phase shift on one signal becomes too large it may cause stability issues in the system. This shift in phase is hard to see in the simulation estimates but is clearer in the estimates from the field test. Figure 10.3 show the numerical estimates from the field tests. Here "numerical" is the high-pass filter method used in this thesis and "comparison" is another numerical estimator based on the definition of the derivative. Both methods were presented in Chapter 3.3. The figure shows that the numerical derivative using the high-pass filter method has a slight phase shift compared to the other method, which was expected. Both methods are also subject to quite a bit of noise. This is a known side effect of these numerical derivatives, as the sensor data is amplified when the numerical derivative is taken. The comparison method

experienced quite a bit more numerical noise compared to the high-pass filter method. The high-frequency noise could potentially be removed with a low-pass filter, but this also introduces a phase shift to the system. The high-pass filter method worked well in the field test as well and was able to give the controllers their missing sensor values.

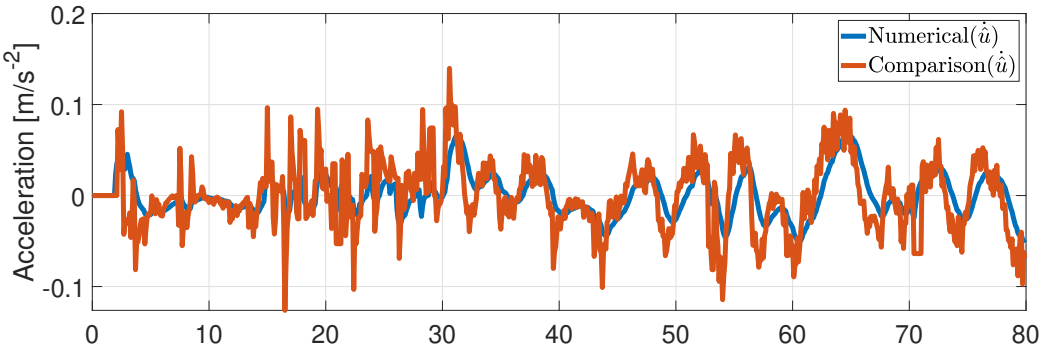

Figure 10.3: Field Test: Numerical Estimates

Overall, the numerical estimation of the lacking sensor data worked. It had satisfactory performance and was able to help the controllers obtain their desired performances. Since there is a slight phase shift and all numerical methods like this produce noise, the solution is not ideal. Potential further work would be to equip the ROV with an accelerometer and a depth velocity sensor. This could potentially perform better than the numerical estimates and give the controllers all the sensor data needed for accurate reference tracking.

10.5 DVL Measurement Obstructions

As mentioned in Section 10.1.2 the velocity references generated by the DVL based guidance system is often oscillating during the field trials, and in some cases, the DVL measurement is completely lost. This is likely a result of the DVL measurements being obstructed by biomass in the net pen. When the DVL measurement is lost the distance measurement is set to zero. Additionally, when DVL measurements are obstructed by objects in the net pen the resulting velocity reference output is sub-optimal. These issues cause a loss in the total system robustness. Since controller performance does not matter if the system is following a faulty reference this issue should be solved.

One way of solving this issue is by estimating the sensor outputs while measurements are offline. Such an estimator was proposed in [21] and a solution was discussed in [22] as further work. Both propose that estimating the desired net heading angle and crosstrack error can allow the ROV to perform accurate operations during signal loss, by using dead reckoning. One issue with these solutions is that estimating the required turning rate for the ROV is challenging. Looking at Figure 8.8 and Figure 9.3 it is clear that the ROV turning rate is not constant in neither simulation nor actual operations. Creating a term to estimate the turning rate dynamics will require the designer to make conservative assumptions in order to make the ROV not collide with the net pen. Therefore, this author

proposes another solution for DVL signal loss.

Once the DVL is unable to provide a measurement the crosstrack error should be estimated, using for instance [23, Equation. (11)] and the system dynamics from Equation (2.3) in an extended Kalman filter. This allows the ROV to close in on its desired distance from the net pen. The heading angle should be held constant on the last measured value, and the guidance algorithm should change to only move the ROV forward in surge. This results in a system that only moves the ROV closer to the net pen during signal loss. Once the desired crosstrack error is achieved the ROV can then use USBL measurements to keep it stationary through dynamic positioning. Once the DVL measurements are back online the ROV can switch back to normal net pen following. This results in a system where the ROV is able to handle signal loss autonomously, with minimal chance of collision.

10.6 Stability Analysis

The stability analysis done in Chapter 7.2 is based on general stability theorems for the GSTA and adaptive GSTA. Additionally, these proofs use assumptions based on the system's mechanical properties. Using these general theorems and assumptions to prove stability was sufficient for this thesis, as the stability was verified through both simulation and field trials in addition to the theoretical proof. Though, potential future work could be to verify the controllers' stability theoretically, without the use of general proofs. This would for the most part be a theoretical exercise with limited practical benefits, but it can give the developer an improved understanding of the controllers' stability conditions.

10.7 Model and Integrator Choices

Two different models were used throughout the development process of this thesis. One simple model was implemented in MATLAB and one complex model was implemented in FhSim. The main difference in the models are the simplifications used, the environmental disturbances acting on the models, and the integration methods used to solve the ODEs.

10.7.1 MATLAB Model

The purpose of the MATLAB model was to do preliminary testing of programs to verify that they function as intended. This model assisted in the early phases of the project as implementing potential ideas and verifying their validity is simpler for the user. This model fulfilled its purpose and worked as intended. Simulating different control strategies, sliding variables, gains, ocean currents, and more was initially done in this model giving the user an idea of how these changes affected the total system performance. The best-performing programs could then be implemented and built into FhSim, where the ideas could be expanded on. This helped streamline the development process as new ideas could initially be tested in a simple development environment giving the author a good

understanding of the theory and how a potential program could be built in C++. The implementation into FhSim was then efficient and with minimal debugging as a general program structure was already created. Therefore, the simplified model implemented into MATLAB was greatly beneficial to the development process.

The MATLAB model uses a simple forward Euler method to solve the differential equations. This integration method was chosen as it is especially simple to implement. The downside of this method is that it is inefficient and should be avoided in solvers where the simulation time matters. This is because the timestep is linearly connected to the error of the solver, meaning that the solver's global numerical error is linearly decreasing with a decreasing timestep [24]. This can potentially result in long simulation times when simulating, as accurate simulations require a small timestep. Additionally, the forward Euler method is an explicit method with a small region of stability [25]. This means that the numerical solver might go unstable if the timestep is too large. For the MATLAB model, this does not matter much, as it is only used for preliminary testing of the controllers and ROV dynamics. Additionally, the simulations done in this thesis are not resource-intensive, as the dynamics are generally slow and only require a few hundred seconds of simulation time. Therefore, sacrificing the solver's efficiency is worth the simplicity of implementation in the MATLAB model. This is acceptable as perfect computational accuracy is not the purpose of the MATLAB model. Additionally, everything done in the MATLAB model is later used in FhSim, verifying the results from the simplified model.

10.7.2 FhSim Model

The purpose of the FhSim model is to accurately verify the controllers' performances. This is done to make sure they function in an environment similar to what they could experience during real-world tests. All software developed was verified through this model, and all simulation results were found using this model. Like all other mathematical models, this model is a simplification of reality. This means deviations will occur in real-world tests. Gains might need to be tuned better, responses might differ from simulation, and test conditions might not be accurately represented in the model. These are problems all simulation models face. The purpose of this model is to minimize the effect of these and provide an acceptable simulation environment able to verify a controller's performance before it is tested in the field. The FhSim model was able to do this properly and was a great resource for software verification throughout the project.

This model used an RK-45 scheme with error estimation. These methods have a much better connection between global error and timestep when compared to the forward Euler method. The RK-4 method is of order four, meaning that if the timestep is halved the global error is divided by four [24]. This exponential reduction in error allows for much lower simulation times without sacrificing the solver's numerical accuracy. The RK-45 method in FhSim allows for adaptive timesteps. This is beneficial for highly nonlinear systems as their dynamics, and therefore the required timestep can vary drastically. To use this in FhSim the user must state a maximum and minimum allowed timestep, and

a relative and absolute error tolerance [18]. Using this can help minimize the simulation time without sacrificing numerical accuracy. For this project, the adaptive timestep functionality was not necessary, and therefore not used. This functionality might be useful for future simulations, or if the controllers are to be used for another, more complex, nonlinear model.

Part V

Conclusion

Chapter 11

Conclusion

This thesis resulted in two GSTA based controller types each with controllers for surge, sway, heave, and yaw allowing for three-dimensional maneuvering of an over-actuated ROV. The controllers developed use two different gain selection methods with their respective benefits and drawbacks. Both controllers were found to be globally finite-time stable using general stability theorems for the GSTA and adaptive GSTA. The fixed-gain version, based on [15], gave reliable results in simulations. It was able to accurately track the net pen in the FhSim simulation environment. The adaptive GSTA controllers, based on [5], was also able to accurately track the net pen in simulation. The controllers' performances were validated through simulation and field tests. The simulation environments created achieved their goals. The MATLAB model helped streamline the development process, and the FhSim simulation environment was able to accurately simulate net pen tracking operations at aquaculture sites. The field test was performed at an exposed fish farm at the SINTEF ACE full-scale aquaculture laboratory, which is the exact environment the controllers were developed to operate in. Overall, the controllers were able to accurately traverse an aquaculture net pen, outperforming conventional PID control in three of the four DOF that were controlled.

The simulation environment created for this project in FhSim worked well. It was able to simulate the conditions and environment seen at exposed coastal sites and allowed for proper verification of the controllers. This was a huge benefit when tweaking the controller design and verifying their performances as the resulting controllers could operate in the field with minimal change. Additionally, the low fidelity model implemented in MATLAB worked well for the initial testing of programs, allowing for a streamlined workflow throughout the software development phase of the project. This means the simulation models fulfilled their purpose and were vital to the controller development process.

The controllers were able to track their references very well in simulation. The gains found were highly effective and the tracking errors for all controllers were minimal. Some sensor data had to be estimated numerically in order to use the desired sliding variables. This was done using a high-pass filter to take the numerical derivative of certain states. This method was able to estimate the lacking sensor data accurately. This resulted in great controller performance during the simulations. The FhSim simulation setup was

made to mimic a net-following operation at a relevant coastal site, meaning the simulations were able to verify that the controllers can follow the net pen as intended. Field tests were performed at the SINTEF ACE full-scale aquaculture laboratory using the ARGUS Mini ROV. These tests were able to verify that the controllers developed could accurately track an aquaculture net pen while affected by significant environmental disturbances. The controller gains found during simulation immediately gave good responses in the field. This meant that only minor tuning was needed to make the controllers track the net pen accurately. Oscillations in the surge and sway DOFs were observed due to the significant environmental disturbances within the net pen. These disturbances were caused by the fish in the net pen, obstructing the sensor view. The controllers were still able to follow their respective references to an acceptable degree of accuracy and the overall tracking of the net pen was a success. Both the fixed gain and adaptive gain GSTA controllers outperformed conventional PID control in every DOF but heave. This shows that the GSTA based controllers are accurate in rough conditions, like the conditions experienced during the testing day. The PID controller had a tough time following the net pen at the desired velocity, resulting in a much slower-moving system.

The author argues that the GSTA controller presented in this thesis is able to withstand the time-varying environmental disturbances that vehicles experience at exposed aquaculture sites. With some further work, these results could lead to an expanded weather window for operations at exposed fish farms.

11.1 Further Work

To further develop the GSTA based controllers' efficiencies a robustness analysis analyzing how the controllers react to extreme conditions and varying parameters or modeling issues can be done. This would give more insight into how the controllers perform during tough conditions and could result in a better understanding of the control laws' operating limits. Such a study could result in better knowledge of what conditions the ROV can operate in with an acceptable degree of accuracy, widening the weather window in which operations can be completed.

The numerical differentiation methods used in this thesis worked well, though they did exhibit some oscillations before converging to an accurate approximation. This issue could potentially be minimized by adding additional sensors to the ROV. This makes these numerical methods unnecessary and might lead to better overall controller performance.

When the DVL is unable to estimate the distance from the vehicle to the net pen the sensor value automatically drops to zero. To increase the total system robustness, an extended Kalman Filter could be designed to estimate the ROV distance from the net. This makes it possible for the ROV to perform dead reckoning while the DVL is offline, increasing the total system robustness.

The theoretical stability analysis done in this thesis is based on a few assumptions and a couple of general theorems. This was sufficient for this thesis, but a more in-depth stability analysis that does not base itself on general theorems could be performed if deemed necessary in the future.

Bibliography

[1] Fiskeridirektoratet. *Totalt salg av slaktet fisk i akvakulturnæringen*. `https://www.fiskeridir.no/Akvakultur/Tall-og-analyse/Akvakulturstatistikk-tidsserier/Totalt-hele-naeringen`. Accessed: 2022-05-29.

[2] H. V. Bjelland, M. Føre, P. Lader, D. Kristiansen, I. M. Holmen, A. Fredheim, E. I. Grøtli, D. E. Fathi, F. Oppedal, I. B. Utne and I. Schjølberg. 'Exposed Aquaculture in Norway'. In: (2015), pp. 1–10.

[3] M. Holmer. 'Environmental issues of fish farming in offshore waters: perspectives, concerns and research needs'. In: *Aquaculture Environment Interactions* 1 (Aug. 2010), pp. 57–70.

[4] W. Caharija. *Artifex Final Project Report - Unmanned surface vessel as a carrier of subsea and airborne vehicles for remoteoperation at fish farms (Artifex)*. 3. Version. 2021.

[5] I.-L. G. Borlaug, K. Y. Pettersen and J. T. Gravdahl. 'The generalized super-twisting algorithm with adaptive gains'. In: *International Journal of Robust and Nonlinear Control* (2022).

[6] T. I. Fossen. *Handbook of Marine Craft Hydrodynamics and Motion Control*. 2nd ed. John Wiley & Sons Ltd, 2021.

[7] G. Antonelli. *Underwater Robots: Motion and Force Control of Vehicle-Manipulator Systems*. Springer, 2006.

[8] H. S. Fadum. 'Control of unmanned subsea vehicles operating at exposed fish farms in presence of time varying environmental disturbances'. Project Report. Norwegian University of Science and Technology, 2021.

[9] S. J. Ohrem. 'Development of a Dynamic Positioning System for Merlin WR 200 ROV'. MSc. Norwegian University of Science and Technology, 2015.

[10] H. B. Amundsen, W. Caharija and K. Y. Pettersen. 'Autonomous ROV Inspections of Aquaculture Net Pens Using DVL'. In: *IEEE Journal of Oceanic Engineering* 47.1 (2022), pp. 1–19.

[11] W. H. Press, S. A. Teukolsky, W. T. Vetterling and B. P. Flannery. *Numerical recipes : the art of scientific computing*. eng. Cambridge, 2007.

[12] J. G. Balchen, T. Andresen and B. A. Foss. *Reguleringsteknikk*. nob. Trondheim, 2016.

[13] R. W. Beard and T. W. McLain. *Small unmanned aircraft: Theory and practice.* Princeton University press, 2012.

[14] Y. B. Shtessel, J. A. Moreno, F. Plestan, L. M. Fridman and A. S. Poznyak. 'Super-twisting adaptive sliding mode control: A Lyapunov design'. In: *49th IEEE Conference on Decision and Control (CDC)*. 2010, pp. 5109–5113.

[15] I. Castillo, L. Fridman and J. A. Moreno. 'Super-Twisting Algorithm in presence of time and state dependent perturbations'. In: *International Journal of Control* 91.11 (2018), pp. 2535–2548.

[16] K.-J. Reite, M. Føre, K. G. Aarsæther, J. Jensen, P. Rundtop, L. T. Kyllingstad, P. C. Endresen, D. Kristiansen, V. Johansen and A. Fredheim. 'FhSIM — Time Domain Simulation of Marine Systems'. In: International Conference on Offshore Mechanics and Arctic Engineering Volume 8A: Ocean Engineering (June 2014).

[17] B. Su, K.-J. Reite, M. Føre, K. G. Aarsæther, M. O. Alver, P. C. Endresen, D. Kristiansen, J. Haugen, W. Caharija and A. Tsarau. 'A Multipurpose Framework for Modelling and Simulation of Marine Aquaculture Systems'. In: International Conference on Offshore Mechanics and Arctic Engineering Volume 6: Ocean Space Utilization (June 2019).

[18] SINTEF Ocean. *The FhSim API.* ver. 2.0.1, Upublished. 2014.

[19] P. Lader, D. Kristiansen, M. Alver, H. V. Bjelland and D. Myrhaug. 'Classification of Aquaculture Locations in Norway With Respect to Wind Wave Exposure'. In: International Conference on Offshore Mechanics and Arctic Engineering Volume 6: Ocean Space Utilization (June 2017).

[20] K. H. Nguyen. 'Control of Unmanned Subsea Vehicles Operating at Exposed Fish Farms in Presence of Environmental Disturbances'. MSc. Norwegian University of Science and Technology, 2021.

[21] P. Rundtop. *Navigation and DP-system tested in fullscale aquaculture net pens.* Project memo. Mar. 2016.

[22] H. B. Amundsen. 'Robust Nonlinear ROV Motion Control for Autonomous Inspections of Aquaculture Net Pens'. MSc. Norwegian University of Science and Technology, 2020.

[23] T. I. Fossen and K. Y. Pettersen. 'On uniform semiglobal exponential stability (USGES) of proportional line-of-sight guidance laws'. In: *Automatica* 50.11 (2014), pp. 2912–2917.

[24] S. Gros. 'Modelling And Simulation, Lecture notes for the NTNU/ITK course TTK4130'. 2021.

[25] O. Egeland and J. Gravdahl. *Modeling and Simulation for Automatic Control.* Jan. 2002.

[26] W. Caharija and P. Rundtop. *ROV6DOF.h.* Revision 3, Closed source, 6 DOF ROV Model for FhSim. 2021.

Appendices

Appendix A

Assumptions and Stability Theorems for the GSTA

Assumption A.1. ***(Continuity Conditions)*** *The functions $\gamma(\sigma,t)$ and $\phi(\sigma,t)$ are Lipschitz continuous functions with respect to t, and $\gamma(\sigma,t)$, $\phi(\sigma,t) \in \mathcal{C}^1$ with respect to σ.* [15, p. 2537] [5, Assumption 1]

Assumption A.2. ***(Bounded Disturbance)*** *The uncertain control coefficient function is assumed to be bounded by positive constraints:*

$$0 < k_m \leq \gamma(\sigma,t) \leq k_M \tag{A.1}$$

[15, p. 2537] [5, Assumption 2]

Assumption A.3. *The perturbation $\phi(\sigma,t)$ can be split into two parts:*

$$\phi(\sigma,t) = \phi_1(\sigma,t) + \phi_2(\sigma,t) \tag{A.2}$$

s.t the first term is vanishing at the origin, i.e $\phi_1(0,t) = 0\ \forall t \geq 0$, and bounded by

$$|\phi_1(\sigma,t)| \leq \alpha|\phi_1(\sigma)|, \quad \alpha > 0 \tag{A.3}$$

[15, p. 2537] [5, Assumption 3]

Assumption A.4. ***(Bounded Growth for ϕ_2 wrt. σ)*** *The total time derivative of the non-vanishing component of the perturbation term divided by the control coefficient $\gamma(\sigma,t)$ can be represented as:*

$$\frac{d}{dt}(\gamma^{-1}(\sigma,t)\phi_2(\sigma,t)) = \gamma^{-1}\frac{\partial\phi_2}{\partial t} - \gamma^{-2}\phi_2\frac{\partial\gamma}{\partial t} + (\gamma^{-1}\frac{\partial\phi_2}{\partial\sigma} - \gamma^{-2}\phi_2\frac{\partial\gamma}{\partial\sigma})\dot{\sigma} \tag{A.4}$$

$$= \delta_1(\sigma,t) + \delta_2(\sigma,t)\dot{\sigma} \tag{A.5}$$

where $\delta_1(\sigma,t)$ and $\delta_2(\sigma,t)$ are bounded by positive constants:

$$|\delta_1(\sigma,t)| \leq \bar{\delta}_1, \quad |\delta_2(\sigma,t)| \leq \bar{\delta}_2 \tag{A.6}$$

[15, p. 2537] [5, Assumption 4]

Theorem A.1. *Suppose that $\gamma(\sigma,t)$ and $\phi(\sigma,t)$ of system $\dot{\sigma}=\phi(\sigma,t)+\gamma(\sigma,t)u$ satisfy assumptions A.1-A.4. Then the states σ_1 and σ_2 converge to zero and z converges to $-\phi(\sigma,t)$, globally and in finite time, if GSTA gains k_1, k_2, and $\beta>0$ are designed as follows. For any $\varepsilon>0$:*

$$k_1>\frac{(1+\varepsilon)}{4\varepsilon k_m}\left(\frac{\alpha}{k_m}(k_M-k_m)+\frac{\bar{\delta}_2\varepsilon}{\beta}(k_M+k_m+2)\right)+\frac{(1+\varepsilon)}{4\varepsilon k_m}\sqrt{\Lambda_{k_1}}+\frac{\alpha}{k_m} \tag{A.7}$$

where

$$\Lambda_{k_1}=\left(\frac{\alpha}{k_m}(k_M-k_m)+\frac{\bar{\delta}_2\varepsilon}{\beta}(k_M+k_m+2)\right)^2+8\varepsilon(k_M-k_m)\left(\frac{\bar{\delta}_2\varepsilon}{\beta}+2\bar{\delta}_1\right) \tag{A.8}$$

, and

$$k_2\in\left(k_M\left(2\sqrt{\underline{h}\varepsilon}\bar{c}-\frac{\bar{c}}{2}\sqrt{\Delta_{k_2}}\right)^2+2\bar{\delta}_1,\ \ k_M\left(2\sqrt{\underline{h}\varepsilon}\bar{c}+\frac{\bar{c}}{2}\sqrt{\Delta_{k_2}}\right)^2+2\bar{\delta}_1\right) \tag{A.9}$$

where

$$\Delta_{k_2}=16\underline{h}\varepsilon-8\left(\frac{(1+\varepsilon)(k_M-k_m)}{\underline{k}_1k_m}\right)\times\left(\frac{(1+\varepsilon)}{\underline{k}_1k_m}\left[\frac{\bar{\delta}_2\alpha}{\beta}+2\bar{\delta}_1\right]+\frac{\bar{\delta}_2\varepsilon}{\beta}+\frac{\alpha}{k_m}\right), \tag{A.10}$$

$$\underline{h}=1-\frac{\bar{\delta}_2}{\beta}\frac{k_m+\varepsilon}{(k_1k_m-\alpha)},\quad \bar{c}=\frac{\underline{k}_1k_m}{(1+\varepsilon)(k_M-k_m)},\quad \underline{k}_1=k_1-\frac{\alpha}{k_m}. \tag{A.11}$$

Moreover, a system trajectory starting at $\sigma(0)=(\sigma_1(0),\sigma_2(0))$ reaches the origin in a time smaller than

$$T(\sigma(0))=\frac{2}{\mu_2}\ln\left(\frac{\mu_2}{\mu_1}V^{\frac{1}{2}}(\sigma_1(0),\sigma_2(0))+1\right). \tag{A.12}$$

[15, Theorem 2.1]

Theorem A.2. *Suppose that $\gamma(\sigma,t)$ and $\phi(\sigma,t)$ in system $\dot{\sigma}=\phi(\sigma,t)+\gamma(\sigma,t)u$ satisfy Assumptions A.1-A.4. Then, the closed-loop dynamics are globally finite-time stable, such that the cases σ_1 and σ_2 converge to zero and z converges to $-\gamma^{-1}(0,t)\phi_2(0,t)$, globally and in finite time, if the gains k_1 and k_2 are designed as expressed in Equation (4.10), $\beta>0$, $\lambda>0$, $\omega_1>0$, and $\varepsilon=\frac{\omega_2}{2\omega_1}\sqrt{\frac{\gamma_2}{\gamma_1}}$, where $\omega_2>0$ and $\gamma_2>0$.* [5, Theorem 1]

Appendix B

ROV6DOF Code Information

The following section of code is taken from [26] and is included to show the assumptions made to create the 6 DOF FHSim ROV model, the features it has, and the sources it uses. The complete program is not publicly available.

```
////////////////////////////////////////////////////////////////////////////////////////////////
/// \class                          ROV6DOF
////////////////////////////////////////////////////////////////////////////////////////////////
//
/// \author         Walter Caharija, Per Rundtop
///
/// 6DOF DP model of Argus Mini ROV. Euler angles used: be aware of the singularites in pitch and roll
/// Model assumptions:
///     - port / starboard symmetric
///     - neutrally buoyant
///     - slow speed maneuvering (< 1 m/s)
///     - CO placed in CG
/// Environmental loads:
///     - Waves and currents can be modelled by external sea environmental model (turn on/off)
///     - Waves can be modelled internally using 2nd order transfer function (turn on/off)
///     - Net cage wake effect can be modelled (turn on/off)
///
/// References:
///     F. Dukan, M. Ludvigsen and A. J. Sorensen, "Dynamic positioning system for a small
///     size ROV with experimental results," OCEANS 2011 IEEE - Spain, Santander, 2011, pp. 1-10.
///
///     Mauro Candeloro, Fabio Dezi, Asgeir J. Sorensen, Sauro Longhi, "Analysis of a Multi -
///     Objective Observer for UUVs," IFAC Proceedings Volumes, Volume 45, Issue 5, 2012,
///     Pages 343 - 348,
///
///     Fossen, T.I. (2011), "Handbook of Marine Craft Hydrodynamics and Motion Control,"
///     John Wiley & Sons, Inc., Hoboken, NJ.
///
///     M. N. Hval, "Modelling and control of underwater inspection vehicle for aquaculture
///     sites", Master thesis, Dept. of Marine Technology, NTNU, Trondheim, Norway, 2012.
///
///     L. Haug, "Hydrodynamic Study of ROV (Remotely Operated Vehicle) Operations at
///     Net - based Fish Farms", Master thesis, Dept. of Marine Technology, NTNU, Trondheim,
///     Norway, 2021.
///
///
/// \par Revision history:
///     Revision 1, 21.09.2018, out for testing, Walter Caharija
///     Revision 2, 20.11.2018, gravity vector added, Walter Caharija
///     (see Example 4.1, Neutrally Buoyant Underwater Vehicles of Fossen, T.I. 2011)
///     Revision 3, 03.11.2021, added wake effect, some renaming of variables, Herman Bjorn Amundsen
///     (see Lars Haugs master thesis from NTNU, 2020)
///
////////////////////////////////////////////////////////////////////////////////////////////////
```

Appendix C

Example: Rougher Environmental Conditions

This subchapter presents data on how the adaptive GSTA controllers used with the ARGUS Mini ROV handles rough environmental conditions. These results are meant as a visual example of what tests and results one could get during a roughness analysis. Normal operations would likely not be done during these conditions, though good controller performance from an in-depth roughness analysis and limit test could widen the operational weather window.

RMSE	
	Adaptive GSTA
Distance:	0.6153 [m]
Heading:	0.0029 [rad]
Surge:	0.0057 [m/s]
Sway:	0.0059 [m/s]
Total Velocity:	0.0059 [m/s]
Depth:	0.0157 [m]

Table C.1: Adaptive GSTA: RMSE Values

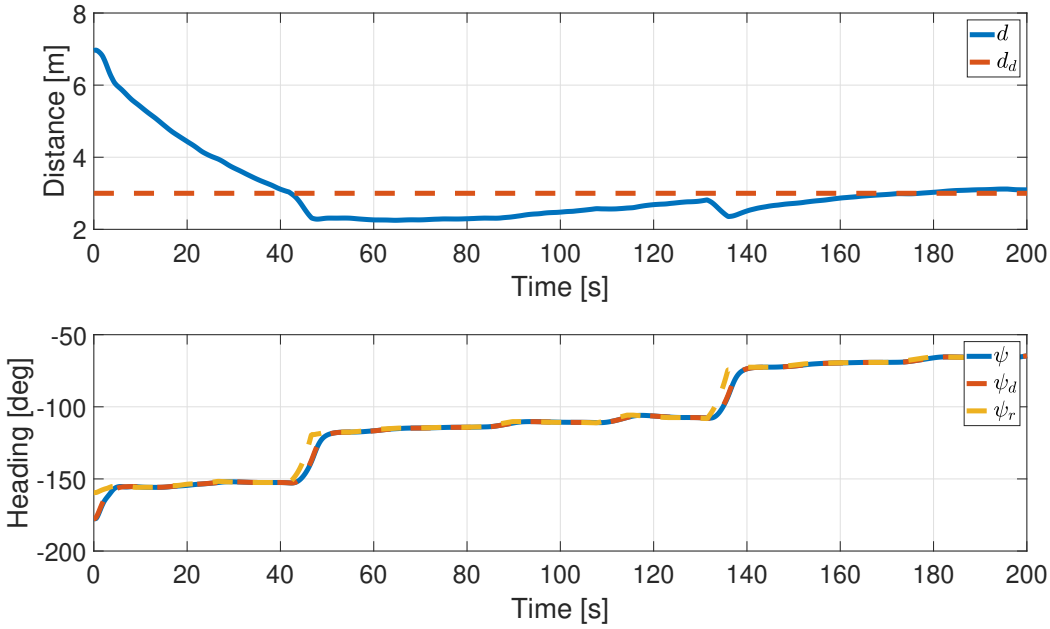

Figure C.1: Adaptive GSTA: Distance and Heading Plots

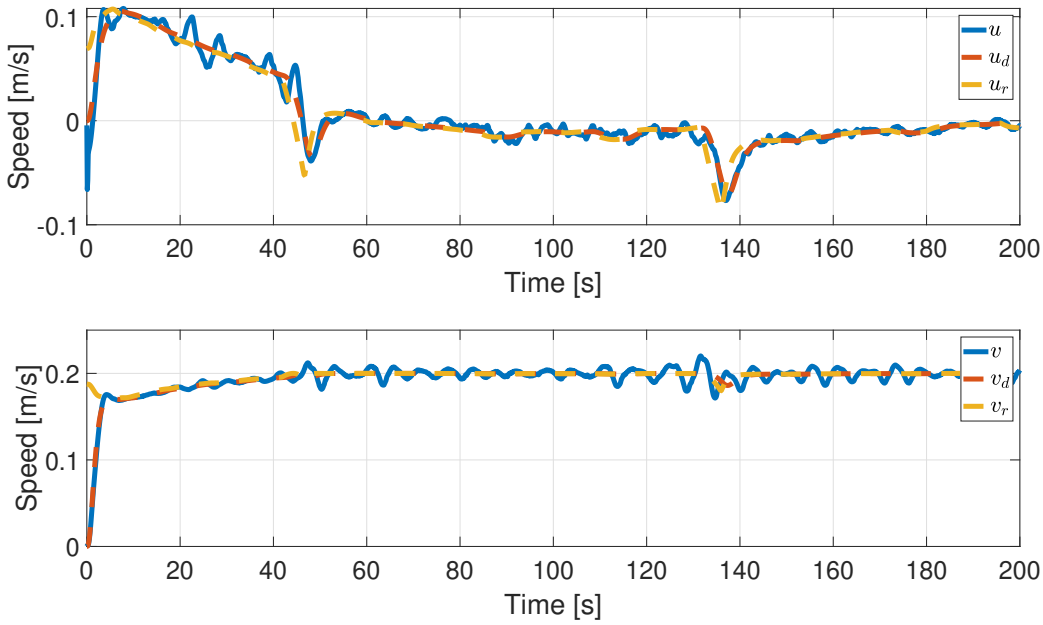

Figure C.2: Adaptive GSTA: Surge and Sway Plots

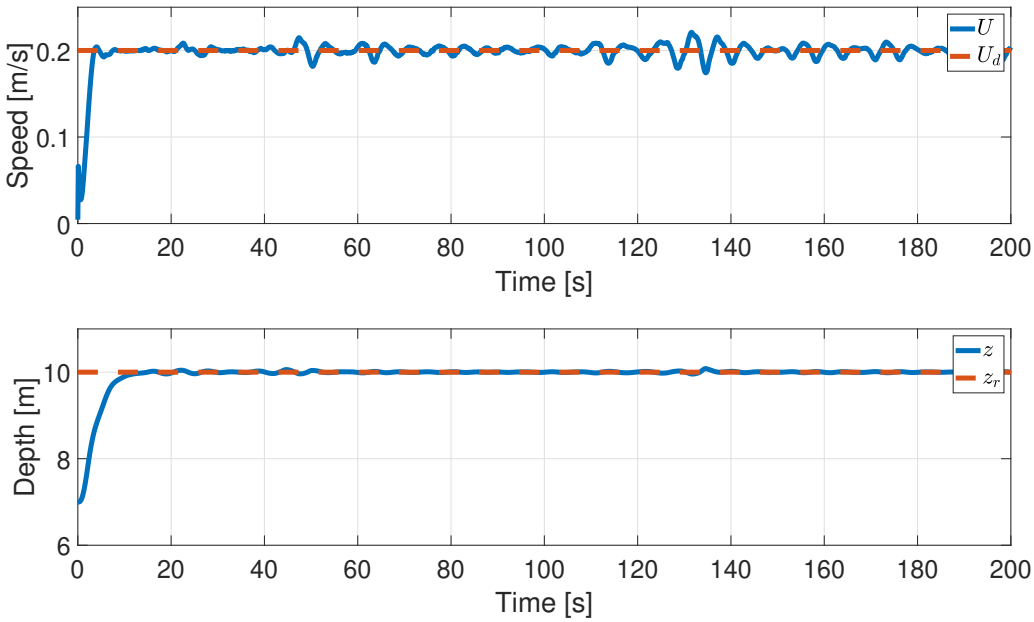

Figure C.3: Adaptive GSTA: Total Velocity and Depth Plots

Håkon Syverud Fadum

Master's thesis

NTNU
Kunnskap for en bedre verden